General Disclaimer

One or more of the Following Statements may affect this Document

- This document has been reproduced from the best copy furnished by the organizational source. It is being released in the interest of making available as much information as possible.

- This document may contain data, which exceeds the sheet parameters. It was furnished in this condition by the organizational source and is the best copy available.

- This document may contain tone-on-tone or color graphs, charts and/or pictures, which have been reproduced in black and white.

- This document is paginated as submitted by the original source.

- Portions of this document are not fully legible due to the historical nature of some of the material. However, it is the best reproduction available from the original submission.

NASA

Technical Memorandum 85037

PLASMA ELECTRON ANALYSIS: VOYAGER PLASMA SCIENCE EXPERIMENT

E.C. Sittler, Jr.

May 1983

National Aeronautics and
Space Administration

Goddard Space Flight Center
Greenbelt, Maryland 20771

PLASMA ELECTRON ANALYSIS:

VOYAGER PLASMA SCIENCE EXPERIMENT

by

Edward C. Sittler, Jr.
NASA/Goddard Space Flight Center
Laboratory for Extraterrestrial Physics
Greenbelt, MD 20771

ABSTRACT

The Plasma Science Experiment (PLS) on the Voyager spacecraft have provided a wealth of data on the plasma ions and electrons in the interplanetary medium and the magnetospheres of the giant planets Jupiter and Saturn. This report presents a description of the analysis used to obtain electron parameters (density, temperature, etc.) from the PLS electron measurements which cover the energy range from 10 eV to 5950 eV. The electron sensor (D cup) and its transmission characteristics are described. A derivation of the fundamental analytical expression of the reduced distribution function F_e is given. This is followed by discussion showing how the electron distribution function f_e, used in the moment integrations, can be derived from F_e. Positive ions produce a correction current (ion feedthrough) to the measured electron current, which can be important to the measurements of the suprathermal electron component. In the case of Saturn, we show that this correction current, which can either add to or subtract from the measured electron current, is less than 20% of the measured signal at all times. Though not shown here, these feedthrough corrections are very important during the Voyager 1 inbound pass through Io's plasma torus. We then briefly comment about the corrections introduced by spacecraft charging to the Saturn encounter data, which can be important in regions of high density and shadow when the spacecraft can become negatively charged.

PLASMA ELECTRON ANALYSIS: VOYAGER PLASMA SCIENCE EXPERIMENT

by E. C. Sittler, Jr.

SECTION 1

INTRODUCTION

The Plasma Science Experiment (PLS) on Voyager is a collection of potential modulated Faraday cups which make both positive ion and electron measurements covering the energy per charge range from 10 eV to 5950 eV. The PLS instrumentation has successfully measured the plasma (ions and electrons) in the interplanetary medium (Sittler and Scudder (1980), Sittler et al. (1981a), Belcher et al. (1981), Gazis and Lazarus (1982), Lazarus and Gazis (1983)), and the magnetospheres of Jupiter (Bridge et al. (1979a,b), Scudder et al. (1981), McNutt et al. (1981), Bagenal and Sullivan (1981) and Saturn (Bridge et al. (1981, 1982), Sittler et al. (1981b), Hartle et al. (1982), Eviator et al., (1982, 1983), Goertz (1983), Sittler et al., (1983), and Lazarus and McNutt (1983)). The Voyager 2 PLS instrument has also played an important role in the detection of Jupiter's magnetotail beyond the orbit of Saturn (Kurth et al. (1981, 1982), Scarf et al. (1981, 1983), Lepping et al. (1982, 1983) and Desch (1983)). In this report we present a fairly detailed description of the electron analysis which has produced the electron parameters (density, temperature, etc.) used in many of the above studies. The analysis described herein is most descriptive of that used for the most recent publication by Sittler et al. (1983) on plasma electrons in Saturn's magnetosphere and is somewhat different from that used and briefly described in Scudder et al. (1981) for Jupiter. The ion analysis, which is fairly straightforward in the solar wind (Bridge et al. (1977), Belcher et al. (1981)) but can be considerably more difficult in the magnetospheres of Jupiter (McNutt et al., (1981) and Saturn (Lazarus and McNutt (1983)) will not be discussed here.

The paper is broken up into 8 sections with the introduction given in Section 1 and a description of the instrument and its operation given in Section 2 (a more complete description is given in Bridge et al. (1977)). Section 3 gives a schematic description of the D cup and its transmission characteristics, followed in Section 4 by a formal derivation of the analytical expression used in our fits to the measured electron spectra; all our parameter estimations, either directly or indirectly, are derived from this expression. We then mention in Section 5 the fitting procedure used in the analysis, which plays an important role in the moment integrations. In Section 6 we expand upon the discussion in Scudder et al. (1981) concerning the moment estimation of electron parameters. Section 7 describes the effect of ion feedthrough corrections upon the electron measurements, which in the case of Saturn, introduce a minor correction to the observed suprathermal component.

Finally, in Section 8 we comment about the effects of spacecraft charging upon the electron measurements.

SECTION 2

INSTRUMENT DESCRIPTION AND OPERATION

The PLS instrument shown in Figure 1 is composed of four potential modulated Faraday cups denoted by the letters A, B, C and D. The three main sensors A, B and C make only positive ion measurements and, except for rare brief spacecraft maneuvers, are always pointed nearly along the spacecraft-Sun line. The side sensor or D cup makes both positive ion and electron measurements and is normally oriented nearly at right angles to the solar direction. The angular response of the side sensor is cylindrically symmetric about its look direction, and provides a field of view with conical half angle $\sim 30^\circ$ (FWHM) about its normal. As shown in Section 3, the D sensor makes differential contiguous measurements of the electron distribution function along the sensor normal. Because the electron thermal speeds are much larger than flow speeds of the plasma, electron measurements are not very sensitive to sensor orientation, unless there are large pressure anisotropies. Since the instrument angular field of view is fairly broad, uncertainties due to pressure anisotropies are not expected to have an important effect upon the analysis.

For cold ions in the solar wind and magnetospheres of Jupiter and Saturn the mach numbers are usually greater than one and the measured currents are sensitive to sensor orientation. During the cruise phase of the mission only the main sensors are sensitive to the supersonic ion component of the solar wind, while the side sensor provides a one-dimensional view of the electrons at nearly right angles to the flow direction. During the encounters with the giant planets, Jupiter and Saturn, the D sensor was aligned to respond to the azimuthally flowing cold ions as much as possible. For most of the inbound portion of the encounter trajectories the D sensor was aligned to view the cold ions; while, except for the Voyager 1 Saturn encounter, the D sensor was not favorably aligned during the outbound passes. During the planetary encounters, the D sensor alignment was such that the center of its field of view generally looked at electrons with pitch angles between 45° and 135°.

Except for the Cruise 1 phase of the mission when electron measurements are made every 12 seconds and only the E1 mode is sampled, the side sensor completes a measurement cycle in 96 seconds during which it passes through the mode sequence M, E1, L and E2. M and L are the high and low resolution positive ion modes, respectively, while E1 and E2 (see Figure 4) are the low and

high energy electron modes, respectively. The energy range for E1 is 10 eV to 140 eV while for E2 it is 140 eV to 5950 eV. Each electron mode is composed of 16 contiguously spaced energy channels; for E2 mode only the upper 12 channels are used (lower 4 channels not useful since suppressor is biased at - 95 volts; see discussion in Section 3). The channels for E1 are nearly equally spaced in energy ($.099 < \Delta E/E < .37$), while for E2 they are more logarithmically spaced ($\Delta E/E = .29$). The sampling time for both energy modes is 3.84 seconds (0.96 second for Cruise 1) and E1 and E2 modes are separated in time by 45 seconds. This large time gap between low and high electron energy measurements can result in discontinuous changes in the composite energy spectrum across the 140 eV boundary joining the two energy modes. Fortunately, this happens only rarely, and the cold and hot components characterizing the electron distribution function within Jupiter's or Saturn's magnetosphere are usually measured by the low and high energy modes, respectively. The ion and electron measurements are never made simultaneously (the shortest time difference between ion and electron spectra is 25 seconds), which may lead to time aliasing problems whenever intercomparisons between ion and electron measurements are made.

SECTION 3
D SENSOR DESCRIPTION AND TRANSMISSION CHARACTERISTICS

The D cup or side sensor is schematically displayed in Figure 2. It has a cylindrical geometry with entrance aperture at one end and collector plate at the other end, and numerous grid meshes in between. The orientation of the side sensor normal relative to the spacecraft coordinate system is shown at the bottom of Figure 2. We have defined the sensor normal such that it points into the sensor and is thus oriented opposite to the sensor look direction. For added information about potential modulated Faraday cups we suggest reading the review article by Vasyliunas (1971) which gives an in-depth discussion of the use of potential modulated Faraday cups for space applications.

The Faraday cup sets up a one-dimensional potential barrier, aligned along the sensor normal, between the modulator grid (grid3) and the ground grid (grid 2) shown in Figure 2. This barrier is only effective for those charged particles having a charge of the same sign as the modulator voltage V_M relative to ground potential. The dc voltage $\bar{V}_M$ defines the energy or speed channel at which electrons are sampled; the superimposed 400 Hz square wave voltage, shown schematically in Figure 2 with amplitude $\Delta\bar{V}_M$, defines the energy or speed channel window size. Note that V_M is negative for electron measurements. The instantaneous current received by the collector is the integrated flux of electrons with velocity component v_n aligned along sensor normal such that

$$\frac{1}{2} m_e v_n^2 > qV_M \tag{1}$$

with

$$V_M = \overline{V}_M \pm \Delta V_M/2 \tag{2}$$

and q = –e for electrons. A current with both a dc and 400 Hz component flows into the collector. Since the amplifiers are ac coupled to the collector, only those electrons satisfying the condition

$$v_{nj-} < v_n < v_{nj+} \tag{3}$$

where

$$\frac{1}{2} m_e v_{nj\pm}^2 = q(\overline{V}_{Mj} \pm \Delta V_{Mj}/2) \tag{4}$$

for speed channel j are sampled. This signal is then amplified, phase detected, and integrated before transmission. The role of the intermediary grids (4, 5 and 6) is mainly to reduce the capacitive coupling from modulator grid to collector plate. The suppressor grids (7 or 8 depending on instrument mode) main purpose is to return secondary electrons emitted by the collector back to the collector. For electron measurements in the E1 and E2 modes, the suppressor voltage V_S is –8 volts and –95 volts, respectively. In the normal suppressor grid configuration (grid 8 is grounded and grid 7 is biased at voltage V_S) the suppressor is not very effective in returning electrons back to the collector. Electron measurements are predominantly made in the normal grid configuration because the instrument is considerably quieter under these conditions (Lazarus, private communication). Preliminary estimates indicate that secondary electron corrections are only 10% for the thermal electrons (secondary electron yields are low), while ~30% corrections are expected for suprathermals. At present these corrections have not yet been incorporated into the electron analysis. Because electrons with energies less than (V_S) cannot penetrate the potential barrier set up the suppressor grid, measurements are confined to energies greater than (V_S). It is for this reason the lower four E2 channels are not useable. We note that the D cup must be oriented at more than 75° from the solar direction, otherwise UV light striking the modulator grid will cause photoemission from the modulator grid, producing a contaminating signal that can swamp the measured current due to the plasma electrons. This problem was only intermittently present during the early phases

of the cruise mission before the Jupiter encounters. Because the spacecraft is stabilized w.r.t. 3 axes, the electron measurements yield only a one-dimensional view of the electron distribution function.

Transmission Function $T(\vec{\nu}; \nu_{nj\pm})$

In order to make a quantitative estimate of electron parameters such as the electron temperature from the measured currents, one must have an accurate determination of the phase space sampled by the sensor. This is given by the transmisison function $T(\vec{\nu}; \nu_{nj\pm})$ for which the index j specifies the speed channel. The transmission function is defined to be that fraction of a monoenergetic unidirectional beam of charged particles uniformly illuminating the entrance aperture which reach the collector plate. Because of cylindrical symmetry of the D cup the angular dependence of T is given solely by the angle of incidence relative to sensor normal θ (see Figure 2). We introduce the normalized response $R(\vec{\nu}; \nu_{nj\pm})$ where

$$T(\vec{\nu}; \nu_{nj\pm}) = T_N R(\vec{\nu}; \nu_{nj\pm}) \tag{5}$$

The constant $T_N = 0.56$ is the normal transmission of the sensor (i.e., $\theta = 0°$) and it is equal to the product of the transparencies of all grid meshes times the ratio of the shielding ring (shown in Figure 2) and aperture cross-sectional areas. In Figure 3 we have plotted a family of curves for the angular response $R(\vec{\nu}; \nu_{nj-})$ as a function of $\theta = \tan^{-1}(\nu_\perp/\nu_n)$. Each curve corresponds to a different speed along sensor normal $\hat{n}$ within the speed window of the lowest E1 speed channel (i.e., $\nu_{n1-} < \nu_n < \nu_{n1+}$). The angular response of R with half width $\sim 30°$ is principally caused by the common overlapping areas of the aperture and shielding ring projected upon the collector at angle θ. The dependence upon ν_n or electron energy, which can be seen to be small, results from the refraction of electron trajectories as they pass through regions of nonzero electric field (e.g., between modulator and ground grids 2 and 4). Furthermore, the angular and energy dependence is essentially independent of speed channel.

Electrons typically have large thermal speeds $\omega_e > 1000$ km/s relative to plasma flow speed $V < 600$ km/s. It follows that the angular width of the electron distribution function f_e seen by the sensor at the one thermal speed level (transverse direction, $\nu_\perp = \omega_e$) will be typically greater than

25° in the lower speed channels. Therefore, the angular width of f_e and R are comparable, resulting in a folding or convolution of instrument response with f_e in the transverse direction relative to sensor normal. This effect is taken into account in the analysis.

In contrast to the broadness of R relative to f_e in the transverse direction, the instrument samples differential slices of f_e along the sensor normal. To show this we present in Figure 4 a plot of the observed reduced distribution function F_e (similar in shape to f_e) measured within Saturn's extended plasma sheet at 1981 238 09:04 SCET by the Voyager 2 spacecraft. The E1 and E2 energy or speed ranges are denoted in the figure; the histogram format is used to indicate the width (Δv_{nj}) of each speed channel with mean speed $\bar{v}_{nj}$. The abrupt change in channel width at 140 eV occurs at the boundary separating the E1 and E2 energy ranges; the fractional window sizes ($\Delta v/v$) for E2 are about a factor of three larger than that for E1. The two component structure of the electron distribution function is clearly demonstrated by this figure. But most importantly, with regard to the analysis, the figure shows the differential character of the measurements in velocity component v_n. Mathematically, this condition of differentiality, which is derived in the next section, is given by

$$\epsilon_j = \frac{1}{6}\left(\frac{\Delta v_{nj}}{\omega_e}\right)^2 << 1 \tag{6}$$

where

$$\Delta v_{nj} = v_{nj+} - v_{nj-} \tag{7}$$

is the speed width of speed channel j. For the speed channels at which the thermal electron measurements are confined (E1 mode), $\Delta v_{nj} \sim 300$ km/s. Referring to Eq. (6), along with the fact that $\omega_e > 1000$ km/s, one finds ϵ_j to be $< 2\%$ for all j; therefore, the E1 measurements are differential along $\hat{n}$. Thus, because the speed channels are so narrow, one can in principle measure electron temperatures less than $10^{4\circ}$ K or 1 ev. In reality this is not always possible, because of the contaminating signal introduced by the suprathermal electrons near the breakpoint energy E_{B1} (see Figure 4). Furthermore, because the measurements are confined above 10 eV, the signal in the lowest E1 channels for temperature $T_e < 1$ eV will be more than 10^{-4} below the peak flux level which occurs at $E < 1$ eV. Therfore, electron densities must be sufficiently high $n_e > 20$ to 300/cm^3 (i.e., exact value depends on I_{TH} or I_N which are variable) with $\phi_{SC} = 0$ volts, if the cold electrons are to produce a signal greater than instrument threshold $I_{TH} \sim 10$ to 10^3 femptoamp or instrument noise $I_N \gtrsim 75$ femptoamps in the first few E1 channels. In the interplanetary medium where

ϕ_{SC} can exceed + 10 volts, a 1 eV low density ($n_e < 1/cm^3$) electron component is detectable whenever spacecraft potentials are this high. The electron measurements in the higher energy mode E2 can also be shown to be differential. At these higher energies (E > 140 eV) the thermal energy of the electrons usually scales with electron energy E (i.e., power law in electron energy or speed); therefore, at 1 keV the thermal speeds ω_e are ∿18,000 km/s. At 1 keV the channel widths $\Delta\nu_n$ are ∿3,000 km/s, so that ϵ_j estimated from Eq. (6) is less than 1%; hence, the E2 measurements are also differential in velocity component ν_n. With these facts in mind, we will now proceed to derive the analytical expression for the reduced distribution function F_e used in our fits.

SECTION 4

DERIVATION OF ANALYTICAL EXPRESSION FOR REDUCED DISTRIBUTION FUNCTION F_e

To begin it is necessary to write down the general expression relating the measured current ΔI_j (ac component) and the electron distriubtion function $f_e(v)$ we are trying to determine. Keeping in mind the definition of the transmission function $T(\vec{\nu}; \nu_{nj\pm})$ and the fact that one can imagine $f_e(v)$ to be a weighted distribution of monoenergetic unidirectional beams of particles incident upon the sensor, it follows that the sampled current ΔI_j is given by

$$\Delta I_j = qAT_N \left\{ \int_{-\infty}^{\infty} d\nu_x \int_{-\infty}^{\infty} d\nu_y \int_{\nu_{nj-}}^{\infty} f_e(\vec{\nu}) R(\vec{\nu}; \nu_{nj-}) \nu_n d\nu_n \right.$$
$$\left. - \int_{-\infty}^{\infty} d\nu_x \int_{-\infty}^{\infty} d\nu_y \int_{\nu_{nj+}}^{\infty} f_e(\vec{\nu}) R(\vec{\nu}; \nu_{nj+}) \nu_n d\nu_n \right\} \tag{8}$$

where A = 100 cm^2 is the cross-sectional area of the entrance aperture, and $\nu_\perp^2 = \nu_x^2 + \nu_y^2$. It can be shown (see Sittler, 1978) that these two integrals can be combined to an accuracy better than 1% yielding

$$\Delta I_j = qAT_N \int_{-\infty}^{\infty} d\nu_x \int_{-\infty}^{\infty} d\nu_y \int_{\nu_{nj-}}^{\nu_{nj+}} f_e(\vec{\nu}) R(\vec{\nu}; \nu_{nj-}) \nu_n d\nu_n \tag{9}$$

Since the measurements are differential along ν_n it is useful to use the mean value theorem for the ν_n integration. Doing this Eq. (9) becomes

$$\Delta I_j = qAT_N \bar{\nu}_{nj} \Delta\nu_{nj} \int_{-\infty}^{\infty} d\nu_x \int_{-\infty}^{\infty} d\nu_y f_e(\nu_x, \nu_y, \nu_{nj}^*) \bar{R}(\nu_\perp^2/\bar{\nu}_{nj}^2; \nu_{nj-}) \tag{10}$$

where we have introduced the mean normalized response

$$\bar{R}(\nu_\perp^2/\bar{\nu}_{nj}^2; \nu_{nj-}) = \frac{1}{\nu_n \Delta\nu_n} \int_{\nu_{nj-}}^{\nu_{nj+}} R(\vec{\nu}; \nu_{nj-}) \nu_n d\nu_n \tag{11}$$

The speed ν_{nj}^* has some value residing between $\nu_{nj\pm}$ where

$$\bar{\nu}_{nj} = \frac{1}{2}(\nu_{nj+} + \nu_{nj-}) \tag{12}$$

is the mean speed for the jth speed channel. If the speed windows are sufficiently narrow, then one can further simplify Eq. (10) by setting $\nu_{nj}^* = \bar{\nu}_{nj}$. In order to estimate the error in making this approximation we made a Taylor series expansion of f_e about $\bar{\nu}_{nj}$ and substituted it into Eq. (9). Doing this, assuming a step function for R in ν_n (good approximation, see Figure 3), using the mean response $\bar{R}$ in place of R, and using a convected-Maxwellian for f_e one gets

$$\Delta I_j = qAT_N \bar{\nu}_{nj} \Delta\nu_{nj} \int_{-\infty}^{\infty} d\nu_x \int_{-\infty}^{\infty} d\nu_y f_e(\nu_x, \nu_y, \bar{\nu}_{nj}) \bar{R}(\nu_\perp^2/\bar{\nu}_{nj}^2; \nu_{nj-}) \left\{1 - \frac{1}{6}\left(\frac{\Delta\nu_{nj}}{\omega_e}\right)^2 \left(1 - \frac{V_n}{\bar{\nu}_{nj}}\right) + \ldots\right\} \tag{13}$$

where $\vec{V}$ is the mean vector velocity of the electrons relative to the sensor coordinate system. Since $V_n < 600$ km/s, and $\bar{\nu}_{nj} > 2000$ km/s, the term $V_n/\bar{\nu}_{nj} \ll 1$ and can thus be dropped. The resulting correction term is identical to that in Eq. (6) where it was shown in general to be less than 2%. The smallness of this correction term means the measurements are differential in ν_n, and the approximation setting $\nu_{nj}^* = \bar{\nu}_{nj}$ has an accuracy better than 2%. Then by noting the fact that $\bar{R}$ is essentially identical for all speed channels, we get the following general expression for the measured

currents

$$\Delta I_j = qAT_N \bar{\nu}_{nj} \Delta\nu_{nj} \int_{-\infty}^{\infty} d\nu_x \int_{-\infty}^{\infty} d\nu_y \, f_e(\nu_x, \nu_y, \bar{\nu}_{nj}) \, \bar{R}(\nu_\perp^2/\bar{\nu}_{nj}^2) \tag{14}$$

with an accuracy better than 2%.

In order to write down an analytical expression for Eq. (14), when for instance f_e is a bi-Maxwellian, we fit the following sum of Gaussians to $\bar{R}$,

$$\bar{R}(\nu_\perp^2/\bar{\nu}_{nj}^2) = A_1 \, e^{-a_1 \nu_\perp^2/\bar{\nu}_{nj}^2} + A_2 \, e^{-a_2 \nu_\perp^2/\bar{\nu}_{nj}^2} \tag{15}$$

The result of this fit is shown in Figure 5, where $A_1 = 0.929$, $a_1^2 = 1.11$, $A_2 = 0.0813$, and $a_2^2 = 19.09$. As can be seen this function gives a very accurate description of $\bar{R}$. Substituting Eq. (15) into (14) and integrating one gets

$$\Delta I_j = \left[qAT_N \pi \bar{\nu}_{nj}^3 \Delta\nu_{nj} \right] \left[\sum_{k=1}^{2} G_{jk} \right] \frac{n_e}{\pi^{3/2} \omega_\parallel \omega_\perp^2} \, e^{-\beta_\perp (\bar{\nu}_{nj} - V_n)^2 (1 - \epsilon_B b_n^2)} \tag{16}$$

where G_{jk} is the integrated response

$$G_{jk} = \frac{A_k \, e^{a_k^2} \left[U_{\perp j}^2 - \dfrac{a_k^2 U_{xj}^2}{\beta_\perp \bar{\nu}_{nj}^2 (1 + \epsilon_B b_x^2) + a_k^2} - \dfrac{a_k^2 U_{yj}^2}{\beta_\perp \bar{\nu}_{nj}^2 (1 + \epsilon_B b_y^2) + a_k^2} \right]}{\sqrt{(\bar{\nu}_{nj}^2 \beta_\perp (1 + \epsilon_B b_x^2) + a_k^2)(\bar{\nu}_{nj}^2 \beta_\perp (1 + \epsilon_B b_y^2) + a_k^2)}} \tag{17}$$

and f_e, assumed to be a bi-Maxwellian, is given by the following expression

$$f_e(\vec{\nu}) = \frac{n_e}{\pi^{3/2} \omega_\parallel \omega_\perp^2} \, e^{-(\beta_\perp (\vec{\nu}_\perp - \vec{V})^2 + \Delta\beta (\nu_\parallel - V_\parallel)^2)} \tag{18}$$

The parameters used in Eq. (16) are defined as follows: (1) $\beta_{\parallel,\perp} = 1/\omega_{\parallel,\perp}^2$, (2) $1/2\, m_e\, \omega_{\parallel,\perp}^2 = kT_{\parallel,\perp}$ where $T_{\parallel,\perp}$ is the electron temperature parallel and perpendicular to $\vec{B}$, respectively, (3) $\epsilon_B = \Delta\beta/\beta_\perp$ is the anisotropy parameter where $\Delta\beta = \beta_\parallel - \beta_\perp$, (4) $U_{\perp j}^2 = (V_\perp/\bar{\nu}_{nj})^2$, $U_{xj}^2 = (V_x/\bar{\nu}_{nj})^2$ and $U_{yj}^2 = (V_y/\bar{\nu}_{nj})^2$ (5) $\hat{b} = \vec{B}/B$ is a unit vector parallel to $\vec{B}$, and (6) n_e is the electron density. If we assume isotropy $\epsilon_B = 0$ (good approximation for thermal electrons) Eqs. (16) and (17) reduce to

$$\Delta I_j = \left[qAT_N \pi \bar{\nu}_{nj}^3 \Delta\nu_{nj}\right]\left[\sum_{k=1}^{2} \frac{A_k\, e^{-(a_k^2 W_\perp^2)/(a_k^2 + \bar{\nu}_{nj}^2/\omega_e^2)}}{a_k^2 + \bar{\nu}_{nj}^2/\omega_e^3}\right] \frac{n_e}{\pi^{3/2}\omega_e^3}\; e^{-\frac{(\bar{\nu}_{nj} - V_n)^2}{\omega_e^2}} \qquad (19)$$

where ω_e is the electron thermal speed and $W_\perp^2 = V_\perp^2/\omega_e^2$. For purposes of simplicity we have approximated the two Gaussian fit Eq. (15) with a single Gaussian $\bar{R} = e^{-a^2(\nu_\perp/\bar{\nu}_{nj})^2}$ shown by the dots in Figure 5 with $a^2 = 1.35$. By doing this Eq. (19) reduces to

$$\Delta I_j = \left[qAT_N \pi \bar{\nu}_{nj}^3 \Delta\nu_{nj}\right]\left[\frac{e^{-(a^2 W_\perp^2)/(a^2 + \bar{\nu}_{nj}^2/\omega_e^2)}}{a^2 + \bar{\nu}_{nj}^2/\omega_e^2}\right] \frac{n_e}{\pi^{3/2}\omega_e^3}\; e^{-\frac{(\bar{\nu}_{nj} - V_n)^2}{\omega_e^2}} \qquad (20)$$

which has an accuracy better than 5% for all speed channels. Finally, dividing both sides of Eq. (20) by $qA\, T_N\, \bar{\nu}_{nj}^3\, \Delta\nu_{nj}$ one gets the reduced distribution function

$$F_{ej} = \frac{n_e}{\pi^{3/2}\omega_e^3}\; e^{-(\bar{\nu}_{nj} - V_n)^2/(\omega_e^2)} \left[\frac{e^{-(a^2 W_\perp^2)/(a^2 + \bar{\nu}_{nj}^2/\omega_e^2)}}{a^2 + \bar{\nu}_{nj}^2/\omega_e^2}\right] \qquad (21)$$

This expression can be generalized to include the energy shift correction introduced by the spacecraft potential ϕ_{SC} where most of the energy change is assumed to occur along the ν_n direction (see Sittler, 1978). Doing this, Eq. (21) has the more general form

$$F_{ej} = \frac{n_e}{\pi^{3/2}\omega_e^3}\; e^{-(\sqrt{\bar{\nu}_{nj}^2 - u_{SC}^2} - V_n)^2/\,\omega_e^2} \left[\frac{e^{-(a^2 W_\perp^2)/(a^2 + \bar{\nu}_{nj}^2/\omega_e^2}}{a^2 + \bar{\nu}_{nj}^2/\omega_e^2}\right] \qquad (22)$$

where $1/2\, m_e\, u_{SC}^2 = e\phi_{SC}$ and $\bar{\nu}_{nj}^2 > u_{SC}^2$.

SECTION 5
FITTING PROCEDURE

The reduction of the integral expression in Eq. (8) to the analytical expression in Eq. (22) has achieved a tremendous simplification of the analysis. Instead of having to evaluate two 3-dimensional integrations for each measurement point in the spectrum during, for example, a model fit to the spectrum, one has only to compute an analytical expression for each measurement point. Look-up table techniques could be used to enhance the computation speed of the analysis based on Eq. (8), but this method, which tends to be less flexible and not as intuitive, would still be slower and require more memory in a computer. As shown in the next section, Eq. (22) also allows one to directly extract f_e from the measurements. In the case where the electron distribution function is well represented by a convected-Maxwellian, estimates of the electron density n_e and temperature T_e can be obtained by fitting the right-hand side of Eq. (22) to the observed reduced distribution function

$$F_{ej} = \frac{\Delta I_j}{qAT_N \pi \bar{v}_{nj}^3 \Delta v_{nj}} \tag{23}$$

In reality, one cannot obtain an estimate of n_e without having some means for estimating the spacecraft potential ϕ_{SC}. In the case of the cruise analysis, the ion analysis was used to give an estimate of the electron density and charge neutrality was enforced. This approach, which gave a direct measure of the spacecraft potential, was used to construct the return current relation presented in Scudder et al. (1981). This return current relation was then used as a constraint equation in the analysis which gave a self-consistent estimate of both the spacecraft potential and electron density. The use of Eq. (22) is also limited by the fact that f_e is not described by a single Maxwellian for the full energy range of the plasma instrument. As discussed extensively in Scudder et al (1981) and Sittler et al. (1983), the distribution function is characterized by a cold and hot component, where the cold component is Maxwellian in form, while the hot component is non-Maxwellian in its energy dependence (see Figure 4). To attack this problem we have fit a sum of three Maxwellians to the reduced distribution function F_e, where Eq. (22) is used for each Maxwellian component. For the spectrum in Figure 4 we have superimposed the result of this three Maxwellian fit to F_e using the x symbol to denote the fit value at each speed channel. A single Maxwellian describes the cold component quite well; two Maxwellians give a fair description of the suprathermals, for which a power law would probably give a better fit. As discussed in the next section, the Maxwellian fits to the hot component are only performed for the purpose of estimating the distribution

function f_e from F_e; f_e is then used in the moment integrations to compute moment estimates of n_e and T_e.

The details of the analysis procedures used to perform these fits can become quite complex because of the wide range of plasma regimes sampled; for example, one must guard against the possible contamination by photoelectrons from the photoelectron sheath surrounding the spacecraft. In most simple terms, the analysis is performed by first fitting a Maxwellian to the cold electrons in the first few speed channels. In the magnetosheath and magnetosphere regions, the flow velocity has been set equal to zero, and in the solar wind the bulk speed from the ion analysis is used. Once this has been done, the breakpoint energy E_{B1} is computed, which is defined to be the energy at which F_e is twice the value of the Maxwellian fit F_{MC} to the cold component F_C (see Figure 4). We then fit a Maxwellian to $F_{H1} = F_e - F_{MC}$ in the third to seventh channels above E_{B1}. The Maxwellian F_{MH1} fit to F_{H1} is then subtracted from F_e in the energy channel below E_{B1} (i.e., $F_C = F_e - F_{MH1}$). We then fit a Maxwellian to this revised F_C and then repeated the same above procedure used to compute E_{B1} and obtain the Maxwellian fit to F_{H1}. A similar procedure is used to get a Maxwellian representation of the hot component F_{H2} above the second breakpoint energy E_{B2}. As can be seen from Figure 4 this procedure yields a good description of the observed reduced distribution function F_e. The Maxwellian fits to the cold electron component are usually very good, on average the goodness of fit parameter $\chi_c^2 \simeq 5$. The χ^2 for the Maxwellian fits to the the suprathermals are larger, being typically greater than 10, but usually give a good estimate of the thermal width of the spectrum over the energy range each Maxwellian component is fit to.

SECTION 6

MOMENTS

As discussed in Scudder et al. (1981) it is desirable to have a quantitative estimate of the total density and mean random energy of the electron gas as a whole, since it is these quantities which appear in the fluid equations. The fitting of a Maxwellian to the distribution function is only useful when it gives a good description of the particle population. Clearly, a Maxwellian does not give a good representation of f_e for the full energy range of the PLS instrument, but does give a good description of the sub-interval of energies occupied by the thermal electrons. The suprathermal electrons are definitely non-Maxwellian; as shown in Section 5, more than one

Maxwellian is needed to describe them. A power law or kappa distribution could be used and would probably give a good but model dependent description of their energy dependence. The reduced distribution function F_e, contrary to f_e which has a direct connection with theory, contains the effects of the instrument function. Furthermore, once f_e is known, it is a relatively simple exercise to integrate over f_e and obtain model independent estimates of the density and temperature of the gas as a whole.

As noted in Scudder et al. (1981) the distribution function f_e can be retrieved from the measurements, so long as the speed window size Δv_n is small compared to the local thermal speed of f_e. By local thermal speed we mean the magnitude of the square root of the local logarithmic derivative of f_e with respect to electron speed. Careful inspection of Eq. (22) reveals that one can estimate f_e from F_e if the distribution function is Maxwellian and the thermal speed ω_e is known. Therefore

$$f_{ej} = f_e(o,o,\bar{v}_y) = F_{ej}(a^2 + \bar{v}_{nj}^2/\omega_e^2) \tag{24}$$

where we have dropped the exponential term with argument proportional to $W_\perp^2$, since for the electrons $W_\perp^2 << 1$. One can carry this approach one step further by saying that f_{ej} can be estimated with Eq. (24) even if f_e is not a Maxwellian at $\bar{v}_{nj}$, by using in place of ω_e in Eq. (24) the locally determined thermal speed $\omega_{ej} = \omega_e(\bar{v}_{nj})$ of f_e at speed $\bar{v}_{nj}$. Note that the correction factor $a^2 + (\bar{v}_{nj}/\omega_e)^2$ is an indication of the angular width of f_e relative to the sensor response R at speed $\bar{v}_{nj}$. Therefore, by estimating the thermal width of f_e along v_n and assuming this gives a good representation of the thermal width of f_e in the transverse direction (isotropy assumption), Eq. (24) should give an accurate estimate of f_e at $\bar{v}_{nj}$. In order to make use of Eq. (24) we must have an estimate of ω_{ej}. Two approaches have been used. In the first approach we make a two point estimate of ω_{ej} from F_{ej} and F_{ej+1} and using Eq. (22). In the second approach we make use of the three Maxwellian fits to F_e to estimate ω_{ej}. Centered on the breakpoint energies E_{B1} and E_{B2} where the thermal speed ω_e has a strong speed dependence, we have linearly interpolated across the breakpoint energies E_{B1} and E_{B2} to obtain an estimate of ω_{ej} in these regions. Both methods yield similar results whenever the signal is well above instrument noise or temporal fluctuations are absent. In the lower density regions or whenever rapid temporal variations are present in the spectra, the first method has problems because the noise or temporal fluctuations introduce localized changes in the slope of F_e which then introduce large errors in the estimation of ω_{ej}. Therefore, we have used the second approach which is less sensitive to noise or temporal fluctuations since the thermal speed is estimated over a broader energy range and more points are used in

estimating the local slope of f_e (i.e., thermal speed estimation less sensitive to single point fluctuations in the energy spectra). One means of checking this procedure for estimating f_e, is to see how well the Maxwellian fits in F_e vs v_n "phase space" compare in f_e vs v_n phase space. If the conversion has been done properly, and the fit to F_e is of a good quality, then the same fit parameters should yield a good match to f_e where

$$f_{ej} = \frac{n_e}{\pi^{3/2} \omega_e^3} \; e - (\sqrt{v_{nj}^2 - u_{SC}^2} - V_n)^2/\omega_e^2 \tag{25}$$

is used for each Maxwellian component. Figure 6, which is the same spectrum plotted in Figure 4 except that f_e is plotted instead of F_e, shows the Maxwellian fits give a good match to both F_e and f_e. For all spectra this comparison has been made we found a similarly good match.

Once the distribution function f_e is known, one can proceed to make moment estimates of the total density n_e and temperature T_e as outlined in Scudder et al. (1981). For reference purposes we write the integral expressions for n_e and T_e, respectively,

$$n_e \cong 4\pi \int_0^\infty f_e(v_d)\, v_d^2\, dv_d \tag{26}$$

$$T_e \cong 4\pi \int_0^\infty f_e(v_d) \left[\frac{1}{2} m_e v_d^2\right] v_d^2 d\, v_d \,/\, (\frac{3}{2} n_e k_B) \tag{27}$$

where

$$v_d = \left[v_o^2 - 2e\phi_{SC} / m_e \right]^{1/2} \tag{28}$$

is the electron speed outside the photoelectron sheath surrounding the spacecraft. The speed v_o is the observed electron speed at the spacecraft surface, e is the unit electric charge, m_e is the electron mass, k_B is Boltzmann's constant, and ϕ_{SC} is the spacecraft potential. The above integrals assume isotropy in f_e where we have taken advantage of the subsonic character of electrons and assumed corrections introduced by pressure anisotropies to be small. As a first approximation, we have only considered the energy shift correction caused by the spacecraft potential in Eqs. (26) to (28). In Sittler et al. (1983) the upper limit used in the integrals 26 and 27 is set by the maximum channel electron fluxes are observed above I_{TH} or $4*I_N$ (I_N is the theoretically estimated

lower limit of the instrument noise; in reality the instrument noise can be greater than I_N), such that the maximum energy of the integral can be no more than 6 keV. Because the bulk of the distribution is below 6 keV within Saturn's magnetosphere, the upper limit for the integrations is essentially infinity. In Scudder et al. (1981) we extrapolated the integrals to infinity, since the suprathermal electrons in Jupiter's magnetosphere were hotter ($T_N \sim$ few keV) and noise in the higher channels less prevalent.

We now amplify the point made in Scudder et al. (1981) concerning the extrapolation down to zero energy. Because the measurements are confined above 10 eV, one must use the estimated temperature T_c for the cold electrons to extrapolate f_e down to zero energy in order to complete the moment integrations. As argued in Scudder et al., this portion of the integral will not make a significant contribution to the integral if f_e does not vary too much below 10 eV or deviate significantly from that indicated above 10 eV. The first condition is violated whenever $T_c < 10$ eV (density dominated by cold electrons) since the integrals will peak near or below 10 eV. Furthermore, as the electron temperatures become lower ($T_c < 3$ eV) most cold electrons have energies < 10 eV, and fluxes above 10 eV can be dominated by suprathermals so that it becomes more and more difficult to make an accurate estimate of T_c. If suprathermals are absent, the cold electron fluxes can be below instrument threshold and/or instrument noise. At these low temperatures, the error in estimating T_c may be no more than a factor of two, but since the spectrum is so steep below 10 eV, large erorrs in the density can result. This accounts for some of the data gaps in the density plots in Sittler et al. (1983), while no data gap is present in the temperature plots; in the same plots other regions have been omitted altogether. Eventually, by using the ion and electron data sets together, the successful analysis in these cooler regions in Saturn's magnetosphere is anticipated.

Another complication arises whenever the temperature of the thermal electrons T_c exceeds $\sim$20 eV, such that a turnover in the spectrum in the lower energy channels tends to occur. That is, the predicted phase density for energies below 20 eV from a Maxwellian fit to energy channels greater than 20 eV, exceeds that observed below 20 eV. This low energy turnover in the spectrum has two possible explanations: (1) we are seeing an effect similar to that seen in the Earth's magnetosheath where the electron distribution function is observed to have a flat topped shape at lower energies; ion acoustic waves have been proposed as the means for providing this distortion of f_e (Dum et al., 1974); or (2) it is an instrumental effect caused by the emission of secondary electrons from the modulator grid. This latter mechanism, first proposed by Vasyliunas (1971) is caused by the change in energy of primary electrons incident upon the modulator

grid as the modulation voltage is varied; by changing their energy the secondary electron yield, which is a function of the primary electron energy, will also change. Then if the flux of electrons is greater at higher speed channels, a significant correction to the lower electron channel is feasible, where this correction current will tend to reduce the measured signal in the lower electron channels (i.e., below 100 eV the secondary yield is an increasing function of primary electron energy). Since the flux maximizes at the electron thermal speed, this effect, if important, will occur whenever $T_c \gtrsim 20$ eV and will affect only those speed channels below ω_e.

Detailed calculations of this effect are being planned for the future. For now we have circumvented this problem by confining our analysis to speed channels above this turnover in the spectrum. If the first explanation applies, then as noted above, we will make only a modest overestimate of the electron density by extrapolating to zero energy the Maxwellian fit to speed channels above the low energy turnover in the spectrum. If it is an instrumental effect, then we make no error by extrapolating to zero energy the Maxwellian fit to speed channels above this turnover in the spectrum.

Since the suprathermal electrons in Saturn's magnetosphere are non-Maxwellian, we have used moment estimates of their density and temperature in our discussions about them in Sittler et al. (1983). As in Scudder et al. (1981) the lower limit of the integration is set by the breakpoint energy E_{B1}; the upper limit is the same as that used for the density and temperature determinations in Sittler et al. Note that this method will tend to underestimate the density n_H and pressure P_H of the hot electrons since we are ignoring their phase density below E_{B1}. This was done to avoid numerical problems which occur if we equate the fractional density n_H to the difference $n_e - n_c$ where n_c is the fit density of the cold electrons. These numerical problems will occur whenever $n_H/n_e \lesssim 0.05$ or when the fit to the cold electrons is poor (which will happen when E1 mode fluxes are near instrument noise). This method is also desirable because it allows one to study more clearly the variations of the more energetic suprathermal electrons above the breakpoint energy E_{B1}. Before the integrations are performed we first subtract the cold component from f_e by using the Maxwellian fit to the cold electrons. Finally, whenever the measured current is below I_{TH} or $4*I_N$, the distribution function f_e is set to equal zero. This approach, which is also used for the n_e and T_e integrations, eliminates the possibility of over estimating the integrals because of noise, while tending to under estimate the integrals because signal less than I_{TH} or $4*I_N$ may be present.

SECTION 7
ION FEEDTHROUGH CORRECTIONS

In Scudder et al. (1981) we made a point that because the instrument records and telemeters only an ac synchronously detected signal, dc background corrections are not a problem. For the high energy particle population this is a correct statement. But low energy positive ions, which have energies per charges < 6 keV comparable in magnitude to the potential applied to the modulator grid of the D cup, will produce an in phase ac signal when the instrument is in the electron mode that may or may not introduce an important correction to the measured electron currents. This feedthrough current I^+_{fed} originally pointed out by Vasyliunas (1971) as a possible correction current, is caused by slight changes in the ion trajectories (see Figure 2) as they pass through regions of nonzero electric field within the sensor (e.g., the modulator grid). When the voltage on the modulator grid is varied at 400 Hz, ions with same energy, angle of incidence, and point of entry will experience slightly different deflections in their trajectories. This will cause some of them to either hit or miss the collector plate (which is ac coupled to the amplifier network) at a 400 Hz rate. The end result, as noted above, is an in phase ac signal to the amplifier network. The sign of this ion feedthrough current I^+_{fed} is such that it will add to the electron current I_e (e.g., $I_{OBS} = I_e + I^+_{fed}$ where I_{OBS} is the observed current).

Using the simulation program developed by Vasyliunas (see Hartle et al., 1982, in which electron feedthrough corrections to the ion measurements were computed) and predicted ion parameters at the spacecraft position from scale height model calculations, we computed estimates of ion feedthrough currents for all electron energy channels throughout a major part of the Saturn encounter period for both Voyager encounters. The results displayed in Figures 7 and 8 show that the observed electron currents due to the thermal electrons are more than two orders of magnitude greater than these correction currents, an expected result. For the suprathermal electrons, for which these corrections have the potential of being important, the feedthrough currents are found to be no more than 20% of the observed signal. As demonstrated in Sittler et al. (1983), the suprathermals contribute about 10% to 20% of the total electron density. It then follows that these feedthrough currents are expected to be important whenever $n_H/n_e \lesssim 1\%$, a situation which is known to occur during the Voyager 1 inbound pass through Io's plasma torus at Jupiter. Since these corrections are only minor at Saturn, we have not included them in the analysis presented in Sittler et al. Whenever the ion analysis is completed, these correction currents will be incorporated into the final electron analysis that is to be part of a future ion and electron paper for Saturn.

You will note that there are occasions at the higher energy channels (channels 25 to 28) when the feedthrough current I_{fed}^{+} exceeds the measured current I_{OBS}. At first thought this is difficult to understand since $I_{OBS} = I_e + I_{fed}^{+}$ should always be greater than I_{fed}^{+}. Focusing our attention on the Voyager 1 data from 0100 to 0400 on day 318 (similar arguments can be made for the Voyager 2 data near the end of day 237), we see that the observed spectra display a strongly energy dependent behavior at higher energies and that signal is confined near or below signal threshold at the higher energy channels (bite-out signatures discussed in Sittler et al. (1981b, 1983)). This should be contrasted with the relatively flat spectrum characteristic of the feedthrough current I_{fed}^{+} produced by the cold ions. We further note that the density profile of the cold ions producing I_{fed}^{+} displays a gradual rise during this same time period (Lazarus and McNutt, 1983), while I_{OBS} for the hot electrons can be quite variable. So the variations in the electron current, which can be quite variable and display a significantly stronger energy dependence than I_{fed}^{+}, cannot be caused by density variations in the ions, but rather are caused by real changes in the hot electron fluxes. The above discrepancy can be understood in terms of a feedthrough current I_{fed}^{-} with sign opposite to that of I_{fed}^{+}, that is produced by ion impact upon the modulator grid with subsequent secondary electron emission from it. This feedthrough current I_{fed}^{-}, based upon preliminary estimates discussed below, is generally small compared to I_{fed}^{+} except at the high energy channels. Therefore, at these higher channels the feedthrough current is expected to be small and possibly negative.

The mechanism producing this negative feedthrough current is similar to that discussed in Section 6, except the incident particles are ions and not electrons. Because the positive ions have polarities opposite to that applied to the modulator grid, all the incident ions are accelerated toward the modulator grid between grids 2 and 3 (see Figure 2). By varying the voltage applied to the modulator grid, the energy at which the ions strike it is varied. Then if the secondary yield is energy dependent, the secondary electron current is also varied. This feedthrough current will be out of phase (negative) with I_e if the secondary yield Y_i is an increasing function of ion energy E_i. For $E_i < 1$ keV the secondary yield Y_i is < 0.1 and essentially independent of E_i (Whipple, 1965). Therefore, for those energy channels the ions strike the modulator grid with $E_i < 1$ keV, the feedthrough current I_{fed}^{-} will be near zero and unimportant.. In the case of tungsten (material grid wires made from) and protons being the incident ion, the yield Y_i is an increasing function of ion energy 1 keV $< E_i \leq 100$ keV (Whipple, 1965). A similar energy dependence is expected for O^{+} ions. Therefore, the feedthrough current I_{fed}^{-} will be negative and reduce the observed current

$I_{OBS} = I_e + I_{fed}^{+} + I_{fed}^{-}$. Because Y_i is an increasing function of ion energy and the energy window size $q_i \Delta V_{Mj}$ increases with V_{Mj} (E2 mode), I_{fed}^{-} will be most important at the higher energy channels for which the ions are accelerated up to energies near 6 keV before striking the modulator grid and secondary yields are approaching 1 ($Y_i = 0.5$ at $E_i = 5$ keV for protons).

In Figure 9, we have plotted I_{OBS}, I_{fed}^{+}, I_{fed}^{-} and $I_{fed} = I_{fed}^{+} + I_{fed}^{-}$ versus channel number for plasma data measured near the Voyager 1 ring plane crossing at Saturn. The ion parameters used to compute I_{fed}^{+} and I_{fed}^{-} were supplied by R. L. McNutt (private communication) for the ion spectrum measured nearly time concident with the electron spectrum. Except for channels 25 to 28, I_{fed}^{+} is less than 20% of the observed current I_{OBS}. I_{fed}^{-} is negligible below channel 22, above which it rises rapidly and exceeds I_{fed}^{+} at channel 28, the uppermost channel. When we combine I_{fed}^{+} and I_{fed}^{-}, the feedthrough current I_{fed} is no more than 10% of I_{OBS}, and the observed variations in I_{OBS} between 0100 and 0400 on day 318 for Voyager 1 and 1930 to 2400 on day 237 for Voyager 2 are most assuredly due to real changes in suprathermal electron fluxes.

SECTION 8

SPACECRAFT CHARGING EFFECTS AT SATURN

The electron analysis for the Saturn and Jupiter data sets uses an empirical return current law to estimate ϕ_{SC}; this law only considers the balance between the photoelectron current emitted by the spacecraft and the incident plasma electron current on to the spacecraft. This approach is sufficiently accurate for electron parameter determinations, so long as the incident plasma electron current outside the sheath is not high enough to enforce a negative potential on the spacecraft. This will happen when the plasma electron current exceeds the photoemission saturation current J_{SAT} as defined in Scudder et al., plus the incident positive ion current and secondary electron emission current. The preliminary estimate for J_{SAT} in Scudder et al., is now estimated to be about a factor of 3 lower, though this estimate will probably require further revision, as we did not take into full account the positive ion current above 6 keV and associated secondary electron emission current. Using this revised value for J_{SAT}, we expect the spacecraft to remain positive in Saturn's magnetosphere so long as electron densities remain below $10/cm^3$ for $T_e = 10$ eV. Since this estimate has not included the ion and secondary electron emission currents, the spacecraft could remain positive for even higher densities and temperatures. Except for the Voyager 1 ring plane crossing period at Saturn this condition is probably met. Detailed comparisons with ion data so

far support this conclusion. It is for this reason we feel the electron analysis of the Saturn data set is in good shape at this time, except for periods of shadow and high density ($n_e > 10/cm^3$) when the spacecraft may have become negatively charged.

REFERENCES

Bagenal, F., and J. D. Sullivan Direct plasma measurements in the Io torus and inner magnetosphere of Jupiter, J. Geophys. Res., 86, p. 8447, 1981.

Belcher, J. W., H. S. Bridge, A. J. Lazarus and J. D. Sullivan, Preliminary results from the Voyager solar wind experiment, Solar Wind 4 at Burghausen West Germany, ed. H. Rosenbauer, 1981.

Bridge, H. S., J. W. Belcher, A. J. Lazarus, J. D. Sullivan, R. L. McNutt, F. Bagenal, J. D. Scudder, E. C. Sittler, G. L. Siscoe, V. M. Vasyliunas, C. K. Goertz, and C. M. Yeates, Plasma observations near Jupiter: Initial results from Voyager 1, Science, 204, p. 987, 1979a.

Bridge, H. S., J. W. Belcher, A. J. Lazarus, J. D. Sullivan, F. Bagenal, R. L. McNutt Jr., K. W. Ogilvie, J. D. Scudder, E. C. Sittler, Jr., V. M. Vasyliunas, and C. K. Goertz, Plasma observations near Jupiter: Initial results from Voyager 2, Science, 206, p. 972, 1979b.

Bridge, H. S., J. W. Belcher, A. J. Lazarus, S. Olbert, J. D. Sullivan, F. Bagenal, P. R. Gazis, R. E. Hartle, K. W. Ogilvie, J. D. Scudder, E. C. Sittler, A. Eviatar, G. L. Siscoe, C. K. Goertz, and V.M. Vasyliunas, Plasma observations near Saturn: Initial results from Voyager 1, Science, 212, p. 217, 1981.

Bridge, H. S., F. Bagenal, J. W. Belcher, A. J. Lazarus, R. L. McNutt, J. D. Sullivan, P. R. Gazis, R. E. Hartle, K. W. Ogilvie, J. D. Scudder, E. C. Sittler, A. Eviator, G. L. Siscoe, C. K. Goertz, and V. M. Vasyliunas, Plasma observations near Saturn: Initial results from Voyager 2, Science, 215, p. 563, 1982.

Bridge, H. S., J. W. Belcher, R. J. Butler, A. J. Lazarus, A. M. Mavretic, J. D. Sullivan, G. L. Siscoe, and V. M. Vasyliunas, The plasma experiment on the 1977 Voyager mission, Space Sci. Rev., 21, p. 259, 1977.

Desch, M. D., Radio emission signature of Saturn immersions in Jupiter's tail, J. Geophys. Res., 88, p. 6904, 1983.

Dum, C. T., R. Chodura, and D. Biskamp, Turbulent heating and quenching of the ion sound instability, Phys. Rev. Lett., 32, p. 1231, 1974.

Eviator, A., G. L. Siscoe, J. D. Scudder, E. C. Sittler, Jr., and J. D. Sullivan, The plumes of Titan, J. Geophys. Res., 87, p. 8091, 1982.

Eviatar, A., R. L. McNutt, Jr., G. L. Siscoe, and J. D. Sullivan, Heavy ions in the outer kronian magnetosphere, J. Geophys. Res., 88, p. 823, 1983.

Gazis, P. R. and A. J. Lazarus, Voyager observations of solar wind proton temperature: 1 – 10 AU, Geophys. Res. Lett., 9, p. 431, 1982.

Goertz, C. K., Detached plasma in Saturn's turbulence layer, Geophys. Res. Lett., 10, p. 455, 1983.

Hartle, R. E. , E. C. Sittler, Jr., K. W. Ogilvie, J. D. Scudder, A. J. Lazarus and S. K. Atreya, Titan's ion exosphere observed from Voyager 1, J. Geophys. Res., 87, p. 1383, 1982.

Kurth, W. S. , D. A. Gurnett, F. L. Scarf, R. L. Poynter and J. D. Sullivan, Voyager observations of Jupiter's distant magnetotail, J. Geophys. Res., 86, p. 8402, 1981.

Kurth, W. S., J. D. Sullivan, D. A. Gurnett, F. L. Scarf, H. S. Bridge, and E. C. Sittler, Jr., Observations of Jupiter's distant magnetotail and wake, J. Geophys. Res. 87, p. 10373, 1982.

Lazarus, A. J. and P. R. Gazis , The radial evolution of the solar wind, 1 – 10 AU, Solar Wind 5 Proceedings, ed. M. Neugebauer, in press, 1983.

Lazarus, A. J., T. Hasegawa and F. Bagenal, Long-lived particulate or gaseous structure in Saturn's outer magnetosphere, Geophys. Res. Lett., in press, 1983.

Lazarus, A. J. and R. L. McNutt, Jr., Low energy plasma ion observations in Saturn's magnetosphere, J. Geophys. Res., in press, 1983.

Lepping, R. P., L. F. Burlaga, M. D. Desch, and L. W. Klein, Evidence for a distant (> 8700 R_J) Jovian magnetotail: Voyager 2 observations, Geophys. Res. Lett., 9, p. 885, 1982.

Lepping, R. P., M. D. Desch, L. W. Klein, E. C. Sittler, Jr., J. D. Sullivan, W. S. Kurth, and K. W. Behannon, Structure and other properties of Jupiter's distant magnetotail, J. Geophys. Res., in press, 1983.

McNutt, R. L., Jr., J. W. Belcher, and H. S. Bridge, Positive ion observations in the middle magnetosphere of Jupiter, J. Geophys. Res., 86, p. 8319, 1981.

Scarf, F. L., W. S. Kurth, D. A. Gurnett, H. S. Bridge, and J. D. Sullivan, Jupiter tail phenomena upstream from Saturn, Nature, 292, p. 585, 1981.

Scarf, F. L., D. A. Gurnett, W. S. Kurth, and R. L. Poynter, Voyager plasma wave measurements at Saturn, J. Geophys. Res., in press, 1983.

Scudder, J. D., E. C. Sittler, Jr., and H. S. Bridge, A survey of the plasma electron environment of Jupiter: A view from Voyager, J. Geophys. Res., 86, p. 8157, 1981.

Sittler, E. C., Jr., Study of the electron component of the solar wind and magnetospheric plasma, Ph. D. dissertation, Mass. Inst. of Technol., Cambridge, Feb. 1978.

Sittler, E. C., Jr. and J. D. Scudder, An empirical polytrope law for solar wind thermal electrons between 0.45 and 4.76 AU: Voyager 2 and Mariner 10, J. Geophys. Res., 85, p. 5131, 1980.

Sittler, E. C., Jr. J. D. Scudder and J. Jessen, Radial variation of solar wind thermal electrons between 1.36 and 2.25 AU, Solar Wind 4 at Burghausen West Germany, ed. H. Rosenbauer, 1981.

Sittler, E. C., Jr., J. D. Scudder, and H. S. Bridge, Detection of the distribution of neutral gas and dust in the vicinity of Saturn, Nature, 292, p. 711, 1981.

Sittler, E. C., Jr., K. W. Ogilvie and J. D. Scudder, Survey of low energy plasma electrons in Saturn's magnetosphere: Voyagers 1 and 2, J. Geophys. Res., in press, 1983.

Vasyliunas, V. M., Deep-space plasma measurements, in Methods of Experimental Physics, Vol. 9B, Plasma Physics, edited by R. H. Lovberg, p. 49, Academic Press, New York, 1971.

Whipple, E. C., Jr. The equilibrium electric potential of a body in the upper atmosphere and in interplanetary space, Ph. D. dissertation, The George Washington University, Washington, D.C., June 1965.

FIGURE CAPTIONS

Figure 1. Photograph of the Voyager Plasma Science Experiment showing the three main sensors A, B, and C and the side sensor D. Contrary to the main sensors, the D cup has the usual cylindrical geometry.

Figure 2. Schematic cross-sectional view of D-cup. Trajectories of incident primary electron and emitted secondary electron are displayed. Figure shows capacitive coupling between collector plate and amplifier chain. Only current ΔI_{ac} is amplified, phase detected and telemetered. Voltage levels indicated for suppressor grid pertain to when the instrument is in E1 mode; when in E2 mode, $V_S = -95$ volts. Angle θ and primary electron normal v_η and transverse $v_\perp$ velocity component axes are shown. The lower left inset shows the orientation of the sensor coordinate axis (X_S, Y_S, Z_S) relative to payload coordinate axis ($X_{S/C}$, $Y_{S/C}$, $Z_{S/C}$). Angles $\theta_\eta = 92°$, $\phi_\eta = 43°$ and $Z_S = -\hat{n}$.

Figure 3. Normalized angular response of D-cup $R(\vec{v}; v_{\eta 1-})$ plotted versus angle of incidence θ. Instrument is in E1 mode, lowest speed channel, and modulator set at lower speed level $v_{\eta 1-}$. Each curve corresponds to electron velocity component $v_\eta(K) = v_{\eta 1-} + \Delta v_{\eta 1}(K/5)$ for K = 1 to 5; the uppermost curve corresponds to K = 5 ($v_\eta = v_{\eta 1+}$). See text for definitions.

Figure 4. Plot of Voyager 2 electron reduced distribution function F_e plotted versus normal component of electron velocity v_η into D-cup. Spectrum measured in Saturn's magnetosphere during outbound pass at L = 8. Histogram format used for data, X's used to denote sum of three Maxwellian fit to data. Cold component F_c, and hot components F_{H1} and F_{H2} are indicated. Breakpoint point energies E_{B1} and E_{B2} defined in Section 5 are denoted as well as speed range covered by E1 and E2 modes. The one telemetry count level (one TMC) and noise level are displayed.

Figure 5. Plot of mean normalized response $R(v_\perp^2/\bar{v}_\eta^2; v_{\eta 1-})$ plotted versus angle of incidence θ of primary electron. _ Mean response computed from normalized response plotted in Figure 3. Actual mean response R terminates at $\theta = \pm 60°$. The two gaussian fit is indicated by the solid curve which exceeds R at $\theta = 0°$ and is non-zero beyond $\theta = \pm 60°$. Circles used to indicate single gausian fit with $a^2 = 1.35$.

Figure 6. Electron speed distribution function f_e (circles) computed from electron reduced distribution function F_e in Figure 4. Cold component f_c and hot components f_{H1} and f_{H2} are denoted; breakpoint energies E_{B1} and E_{B2} are also indicated. Solid curve displays sum of three Maxwellian fit to data in Figure 4 (see Section 5). One telemetry count level (one TMC) and noise level are displayed.

Figure 7. Plot versus time of the measured electron current I_{OBS} and predicted ion feedthrough current I_{fed}^+ for all 28 energy channels (channels 1 to 16 for E1; channels 5 to 16 for E2); currents are in femptoamps. The data was measured during the Voyager 1 encounter with Saturn. The ion parameters are computed from a scale height model calculation; uncertainties in composition are not expected to produce significant errors in our estimation of I_{fed}^+. The data plotted with an X symbol at 0406 day 318 were computed from ion parameters determined from a detailed fit to the ion spectrum at this time (ion parameters provided by R. L. McNutt, private communication). As can be seen the model and fit ion parameters yield nearly identical results. Noise and one telemetry count (TMC) levels are also displayed.

Figure 8. Same as Figure 7 except Voyager 2 Saturn encounter data are used.

Figure 9. Observed electron current I_{OBS} (solid line) and ion feedthrough currents I_{fed}^{+} (dotted line), I_{fed}^{-} (short dash) and $I_{fed} = I_{fed}^{+} + I_{fed}^{-}$ (long dash) plotted versus channel number for the Voyager 1 electron spectrum measured at 318 04 06 SCET; currents are in femptoamps. The feedthrough current I_{fed} represents an upper estimate, but is probably correct within a factor of 2.

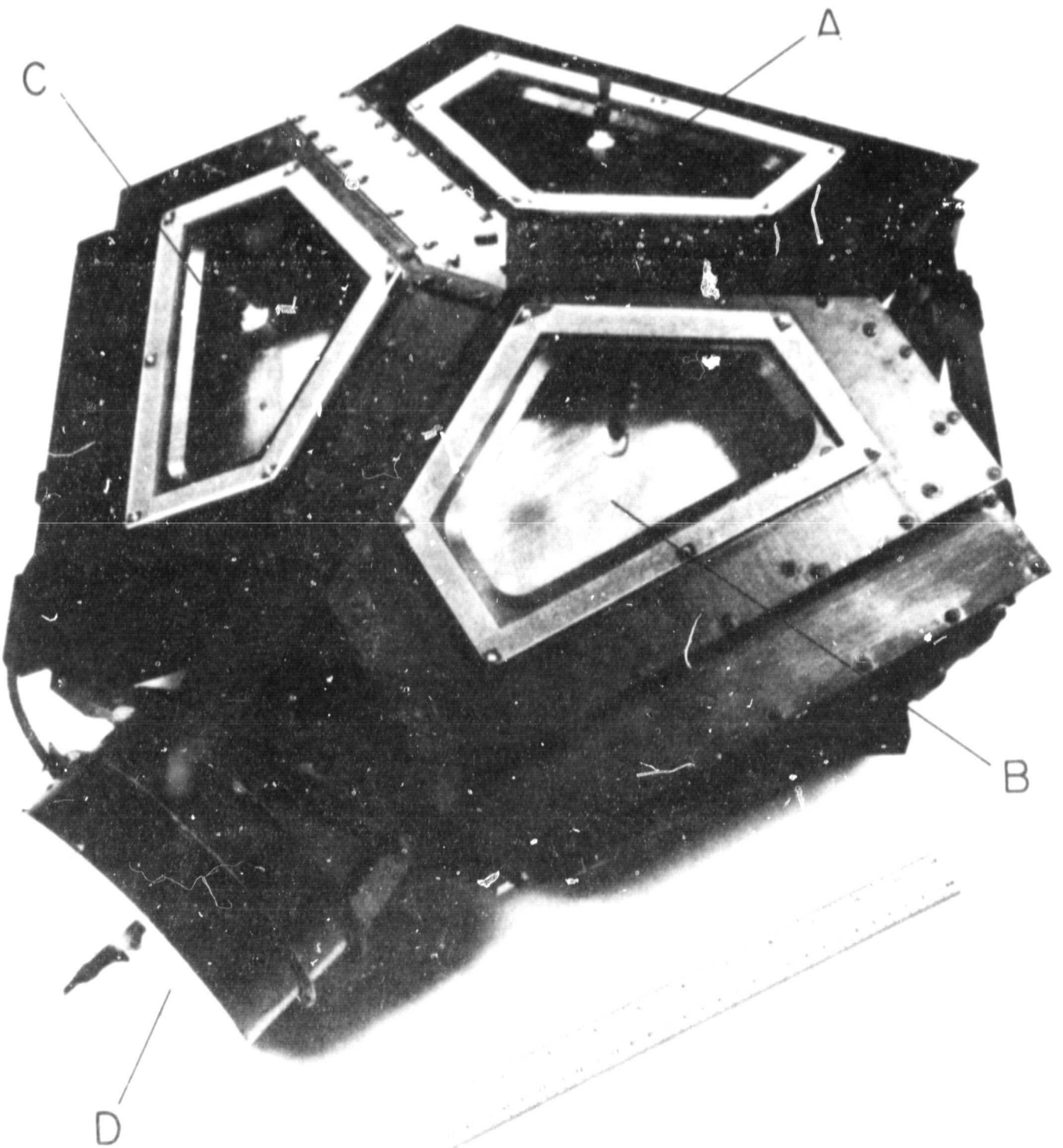

Figure 1

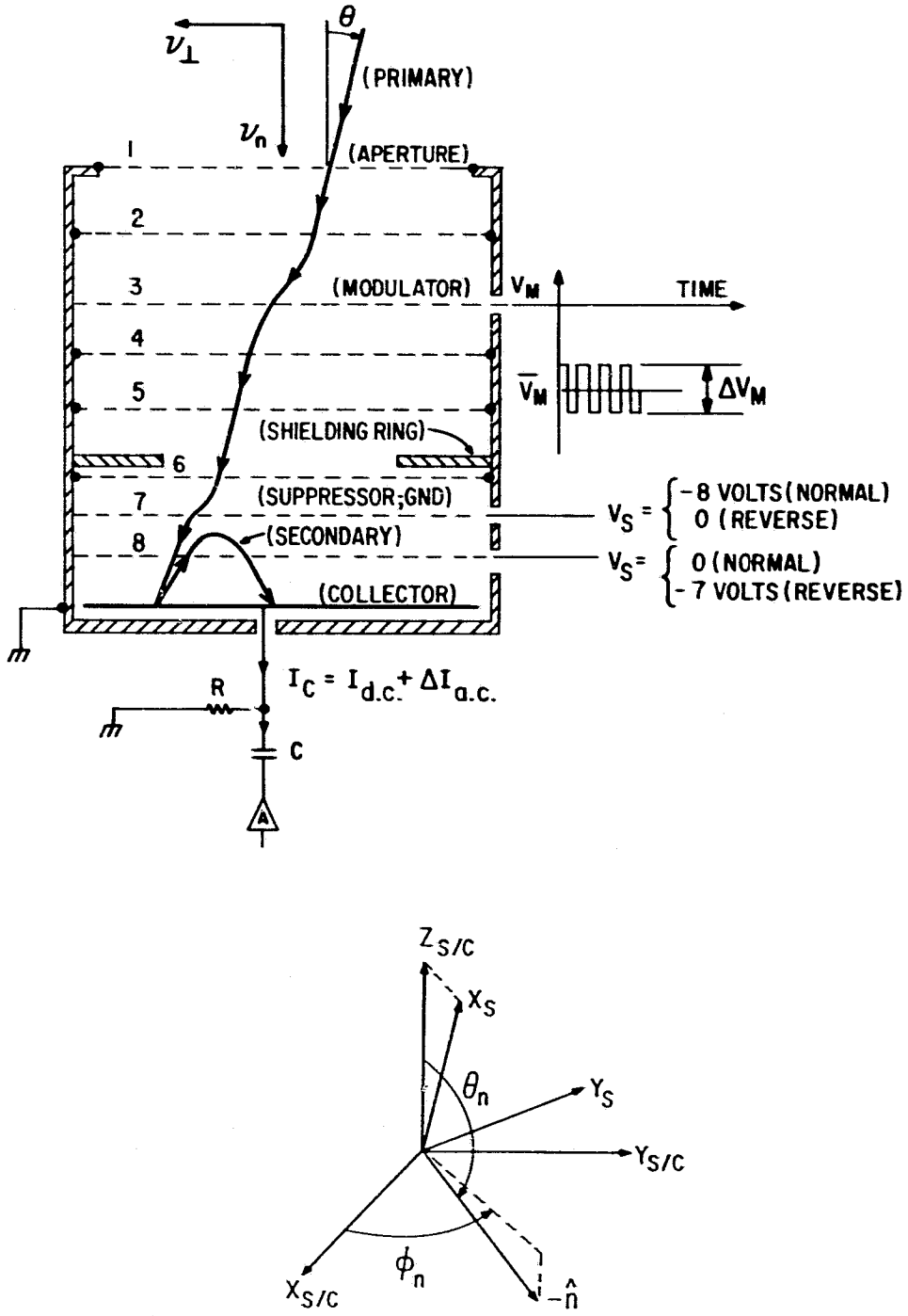

Figure 2

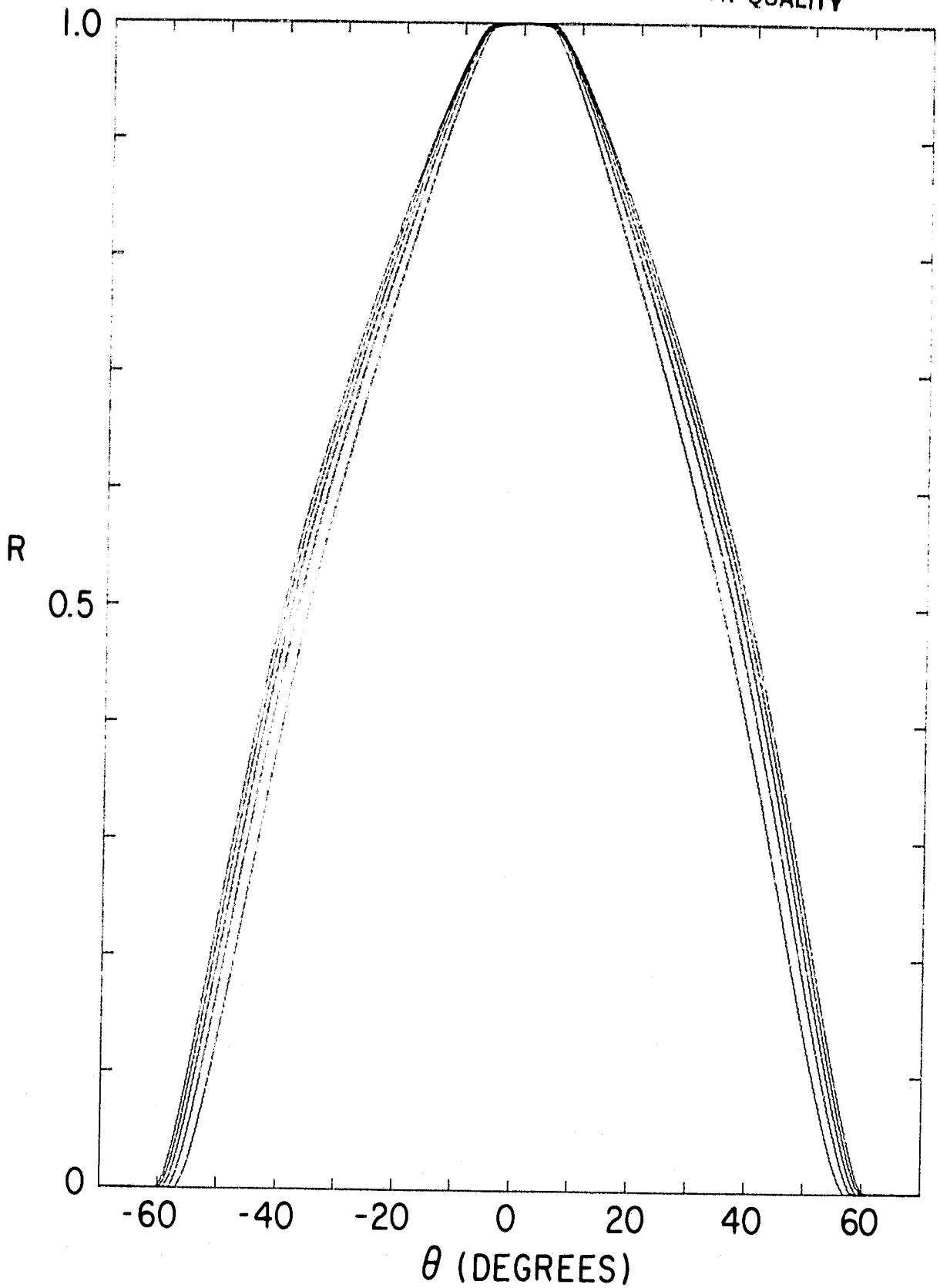

Figure 3

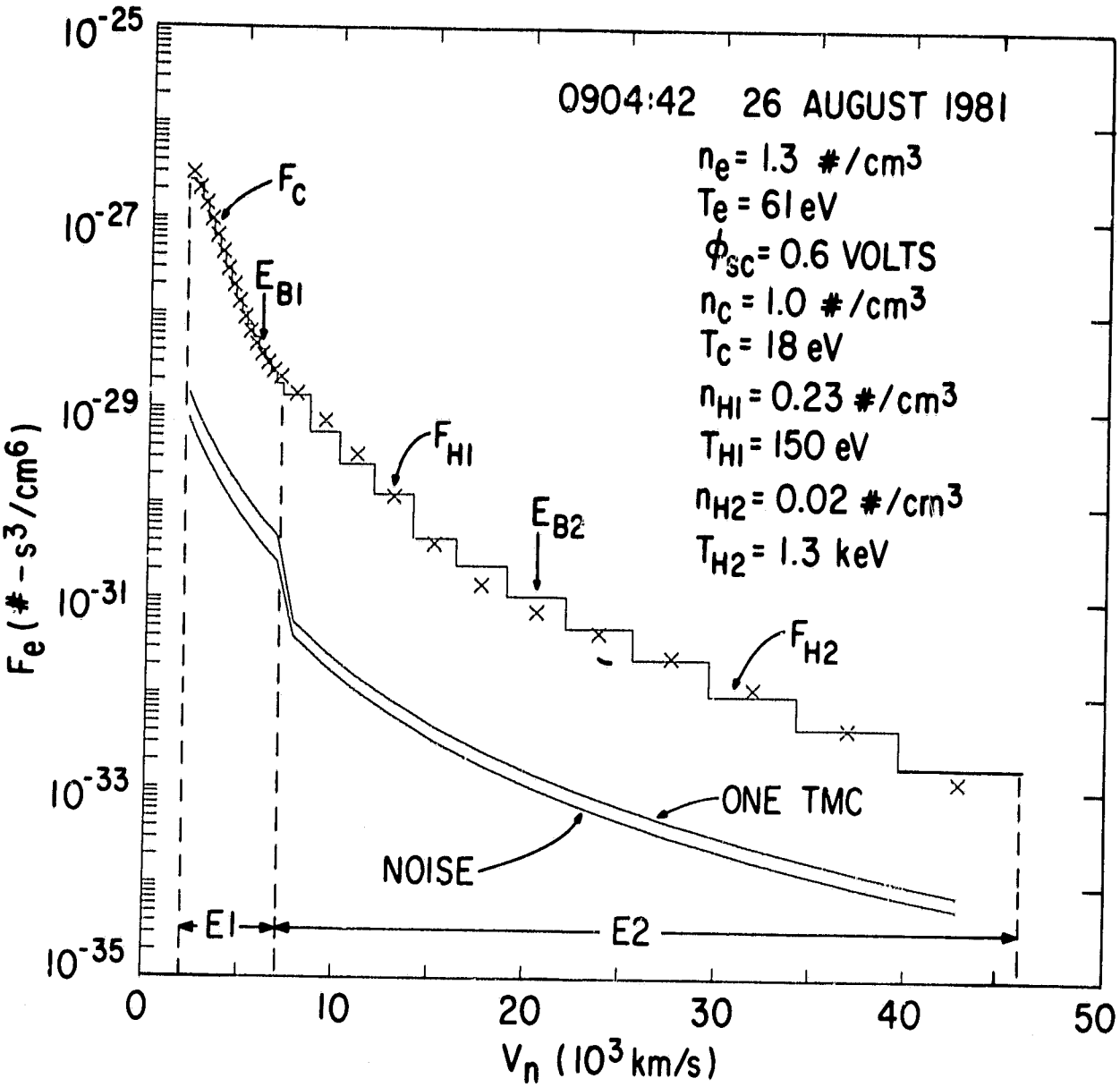

Figure 4

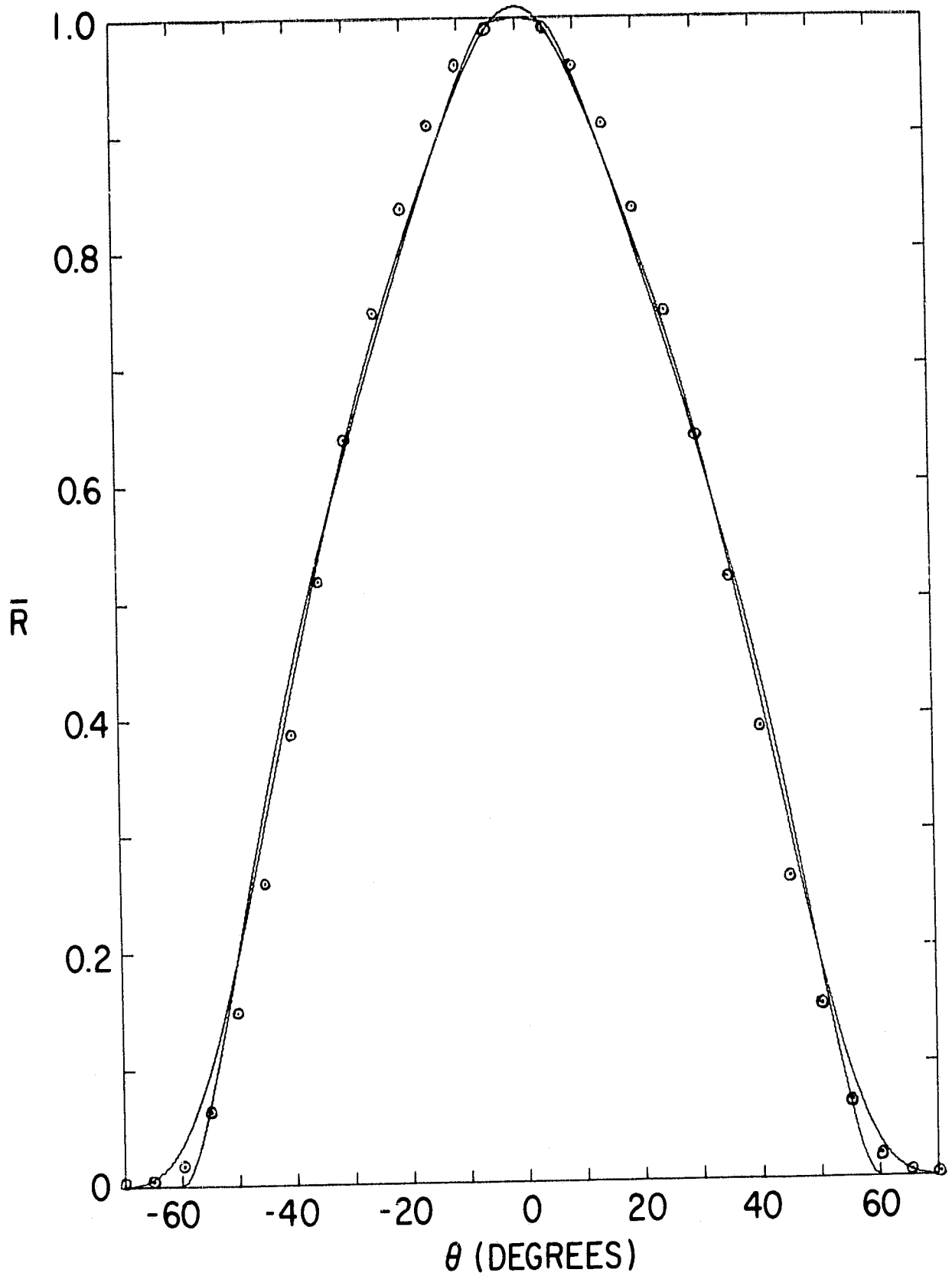

Figure 5

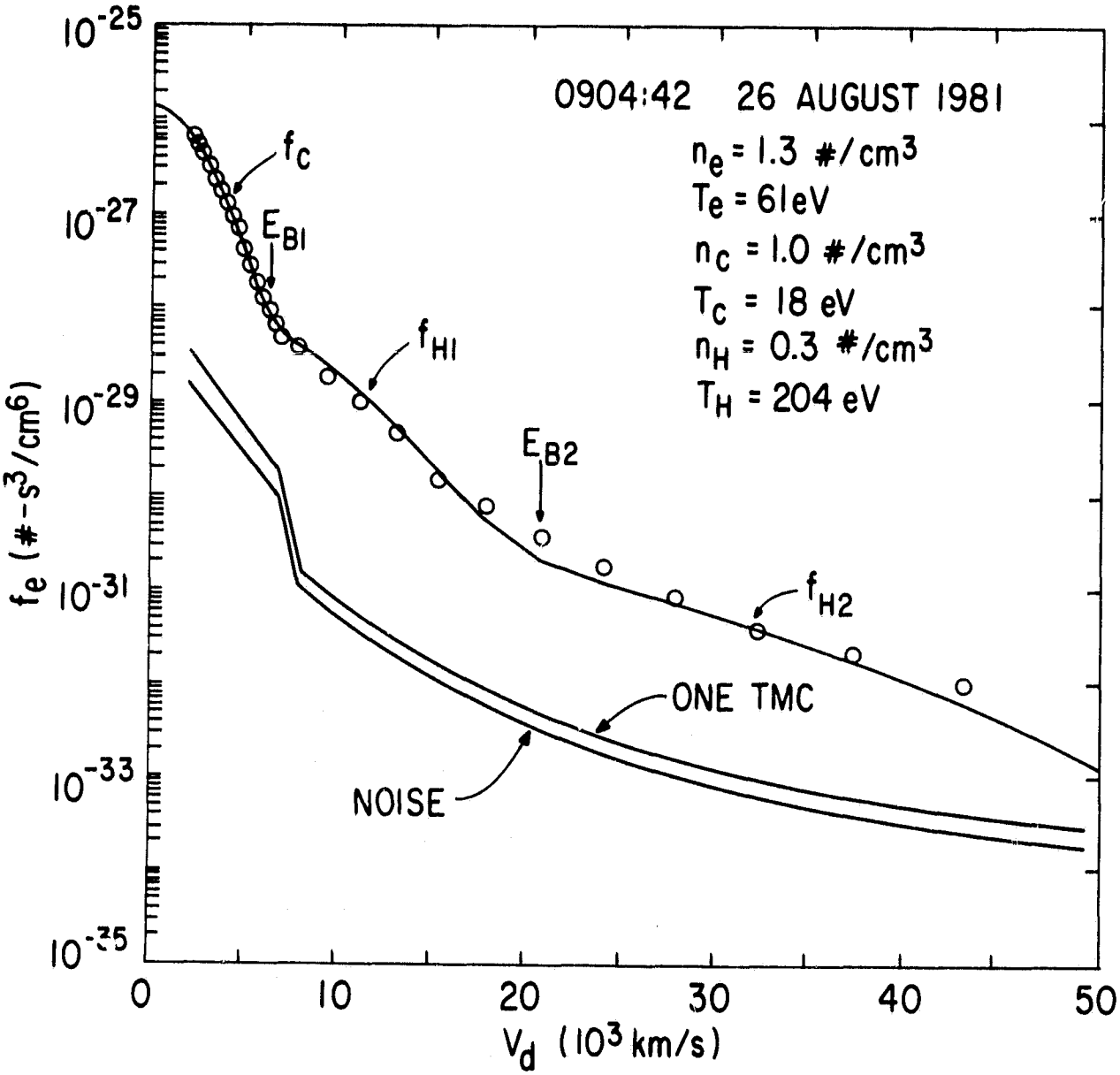

Figure 6

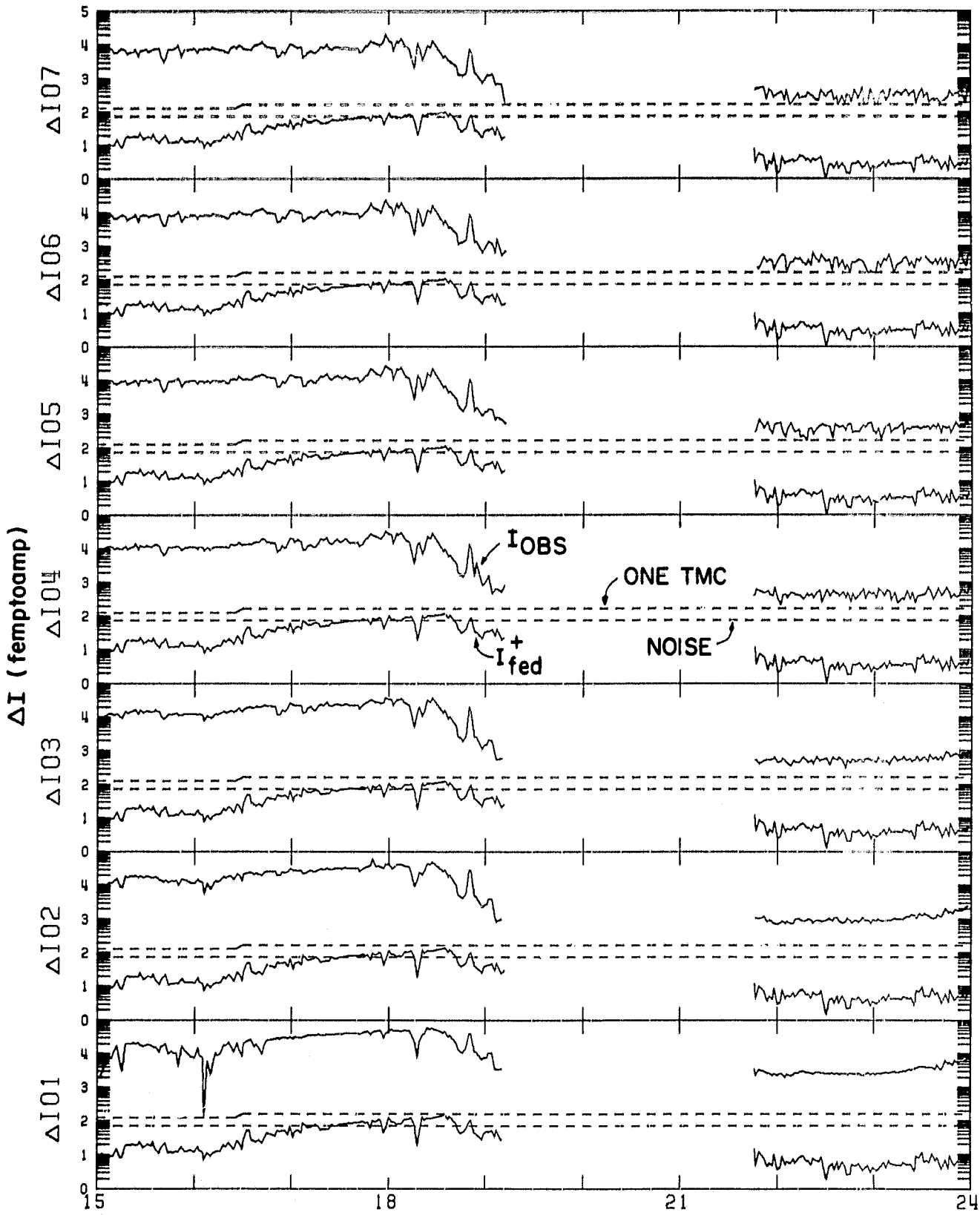

Figure 7a

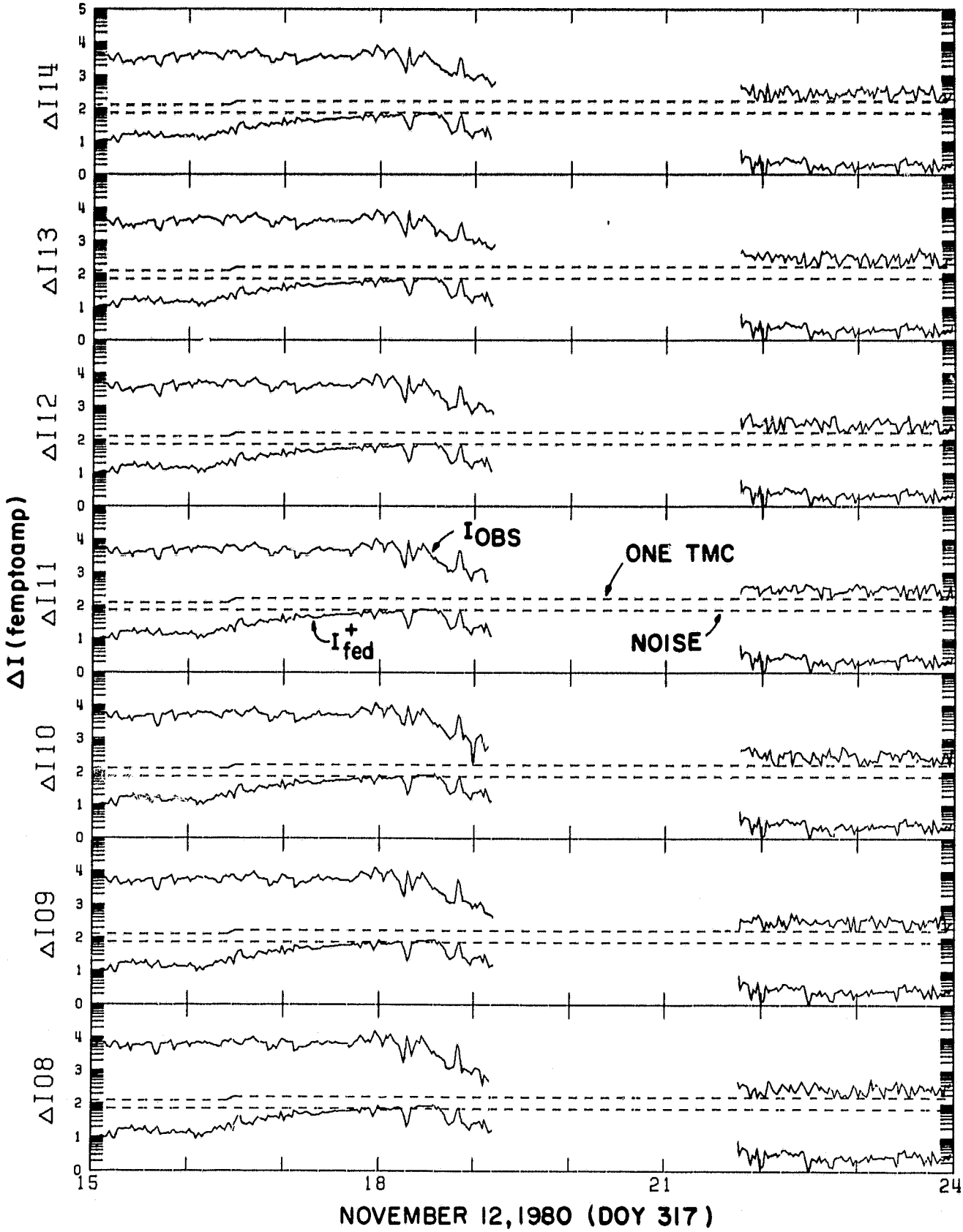

Figure 7b

ION FEEDTHROUGH V-1

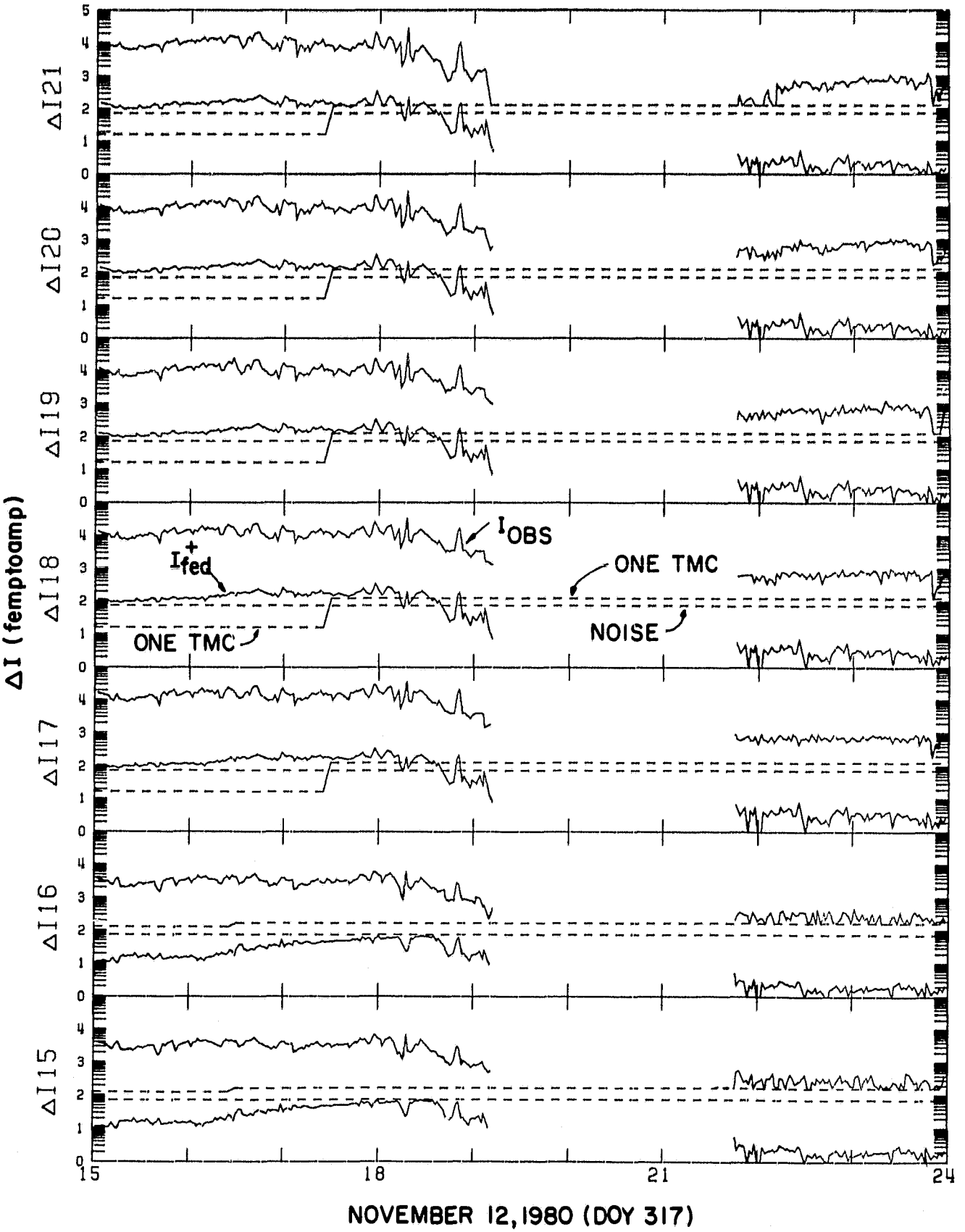

Figure 7c

ION FEEDTHROUGH V-1

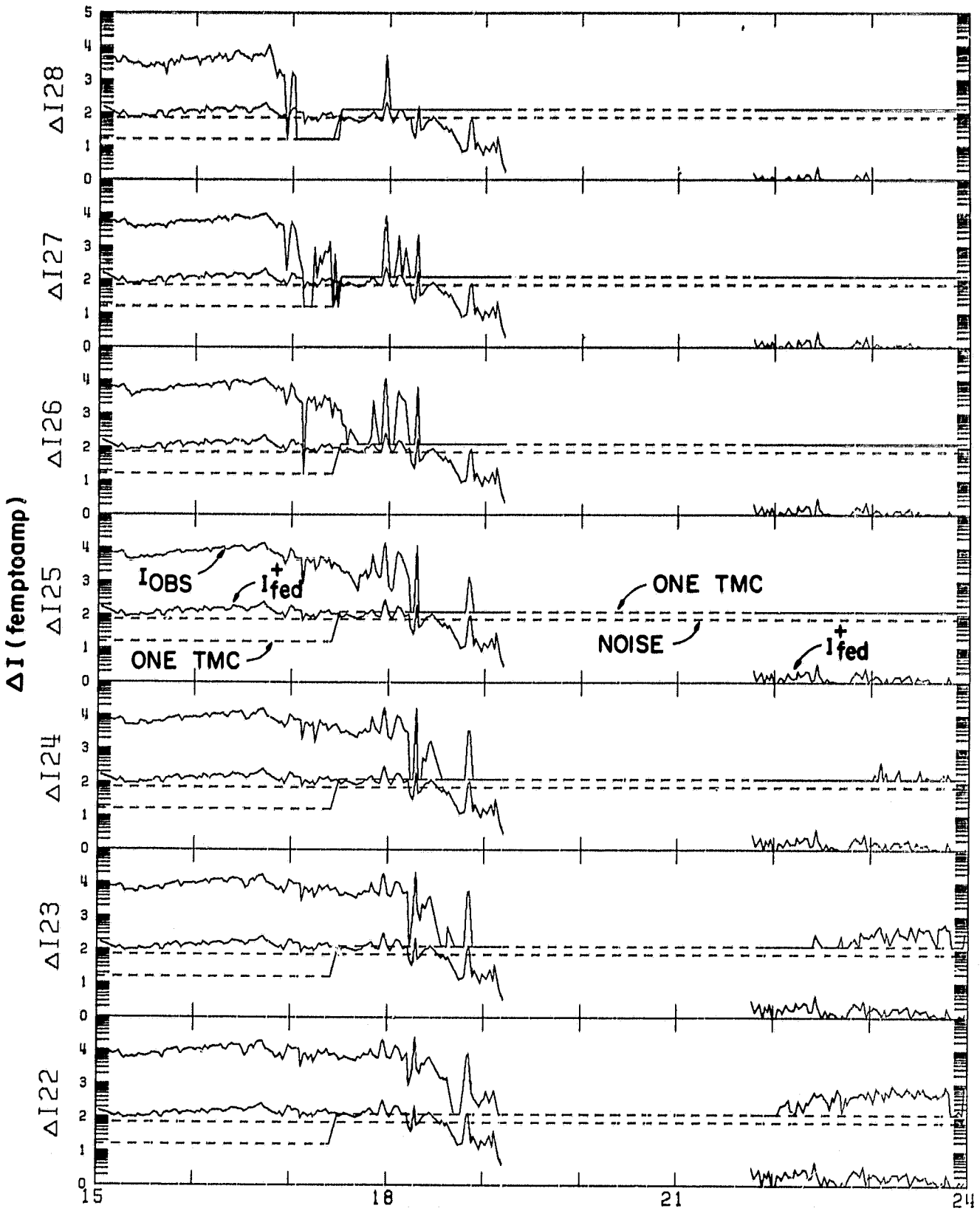

Figure 7d

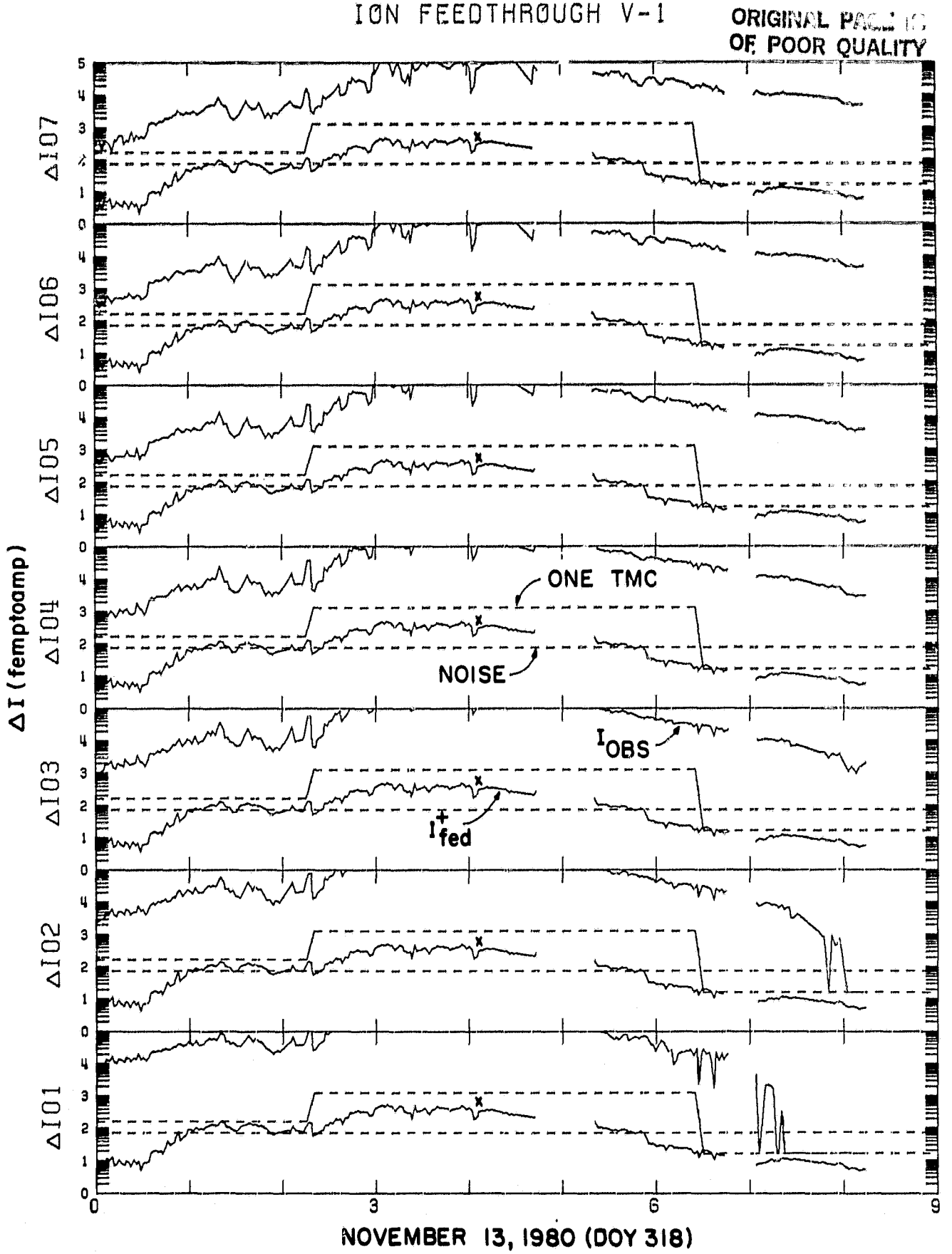

Figure 7e

ION FEEDTHROUGH V-1

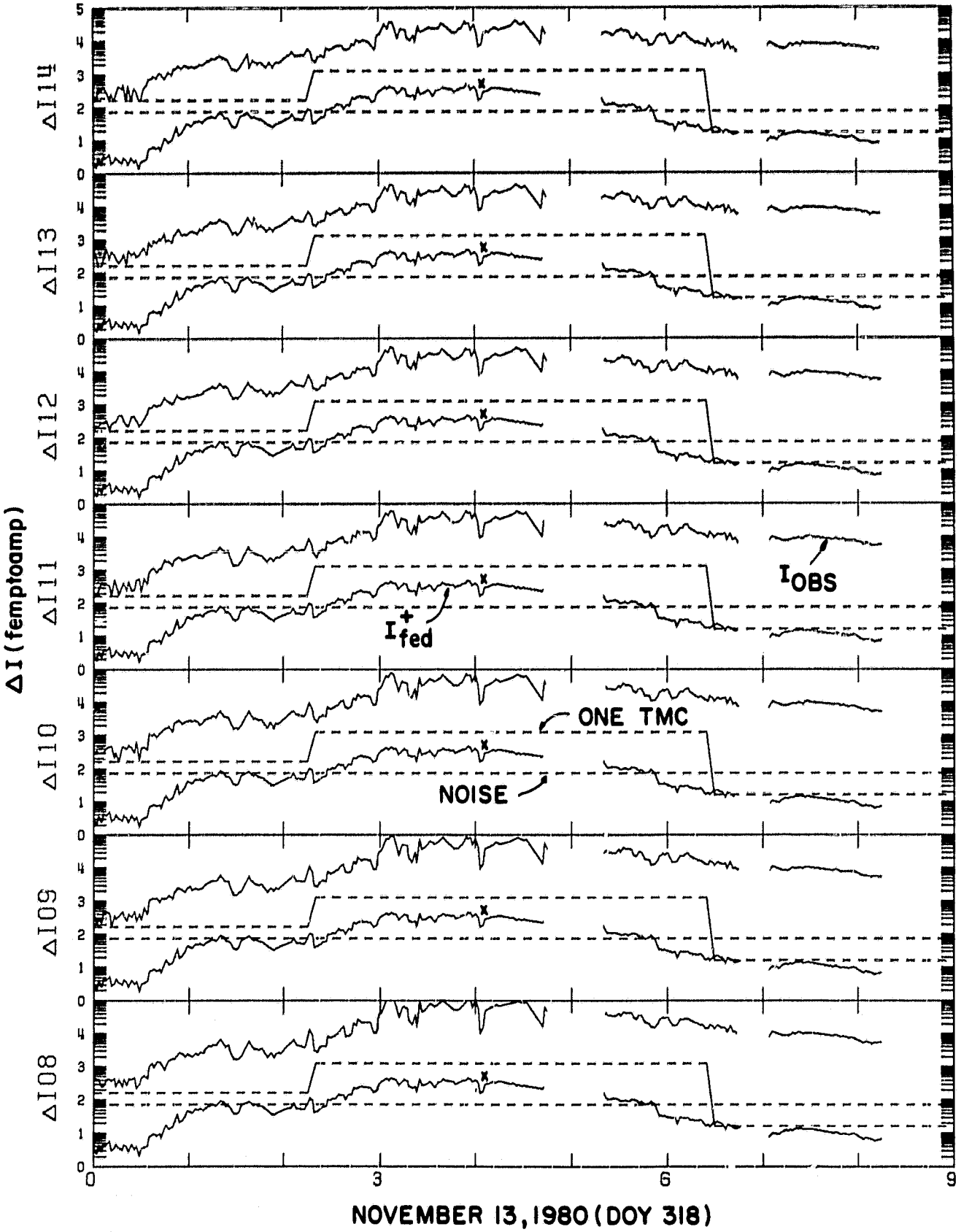

Figure 7f

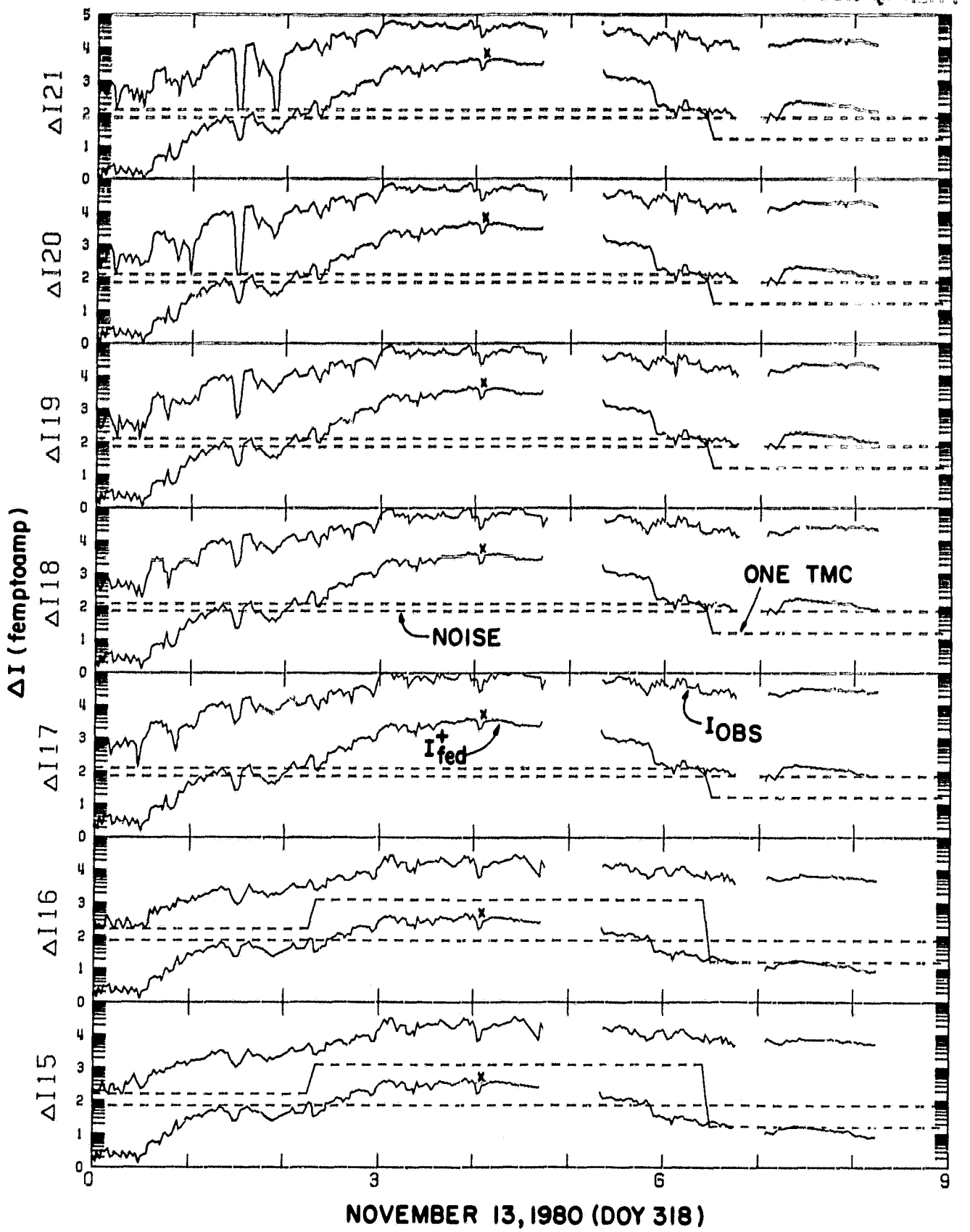

Figure 7g

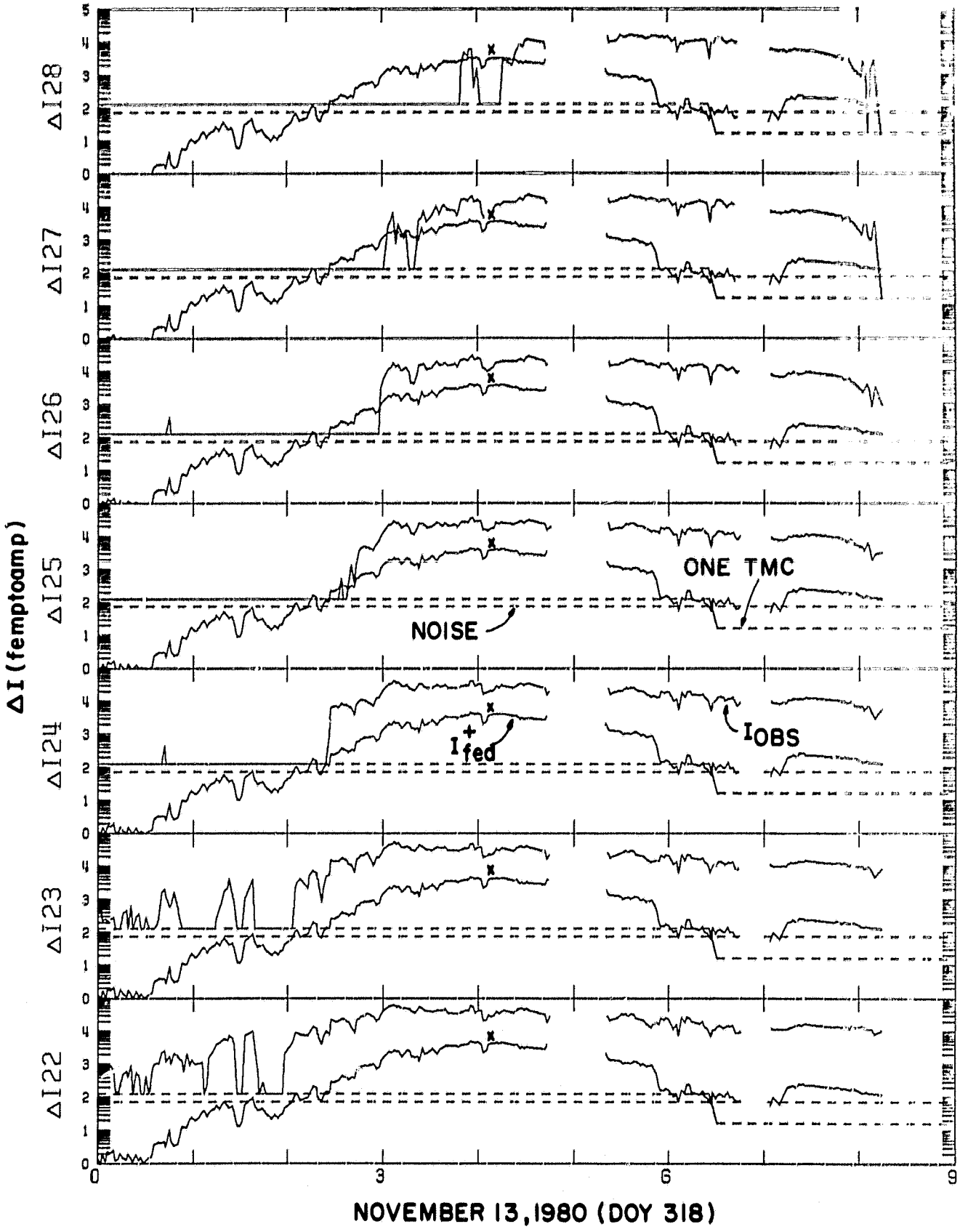

Figure 7h

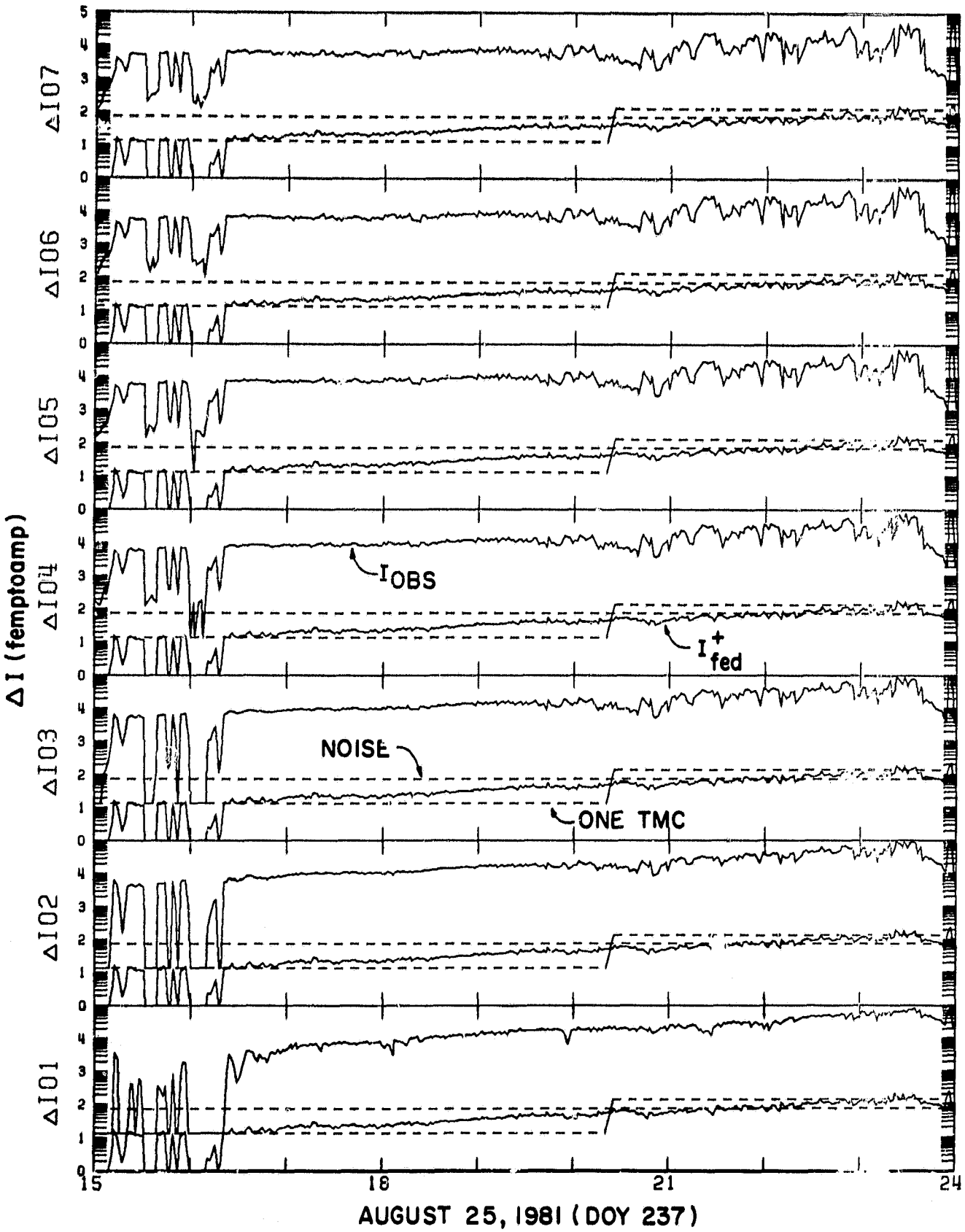

Figure 8a

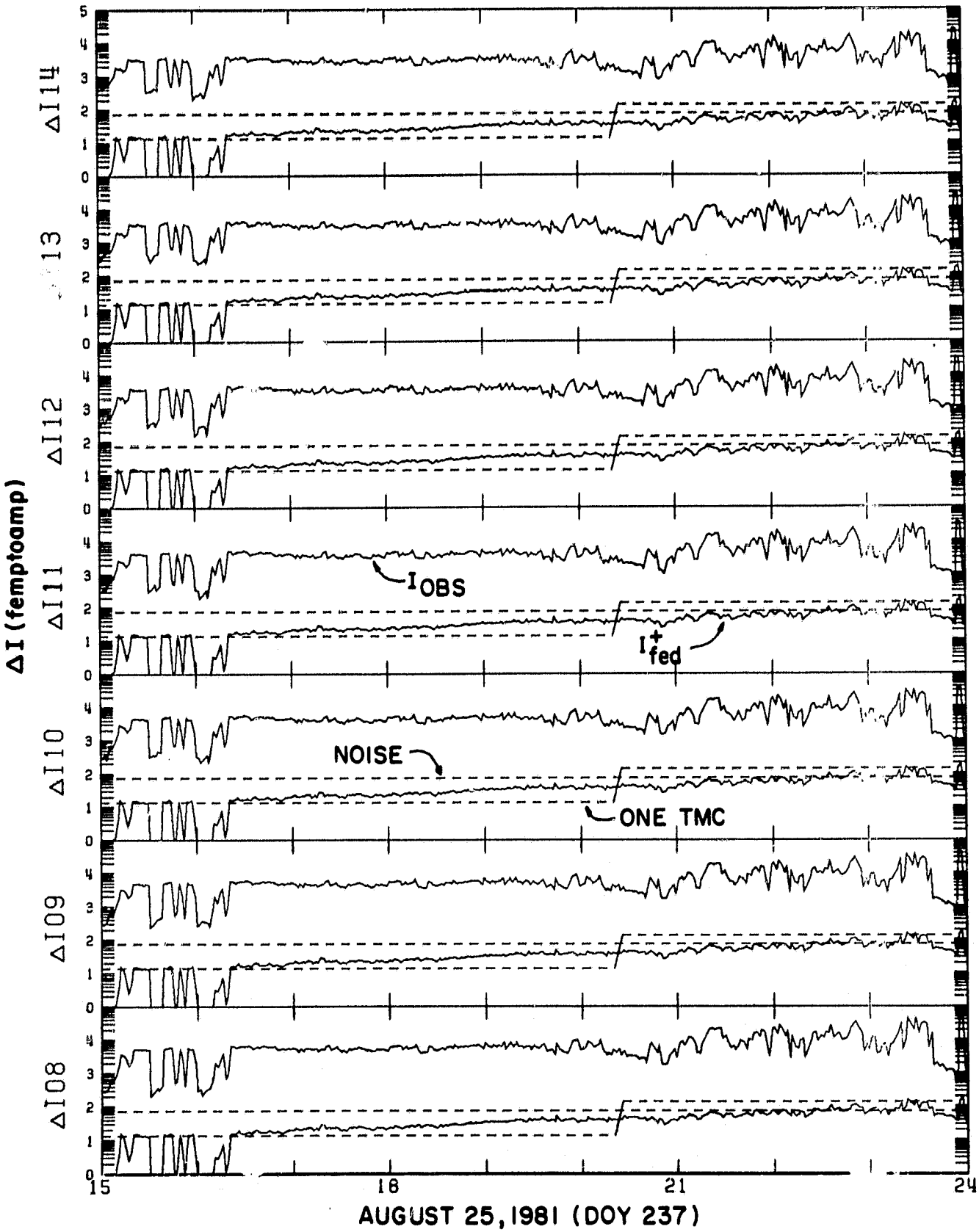

Figure 8b

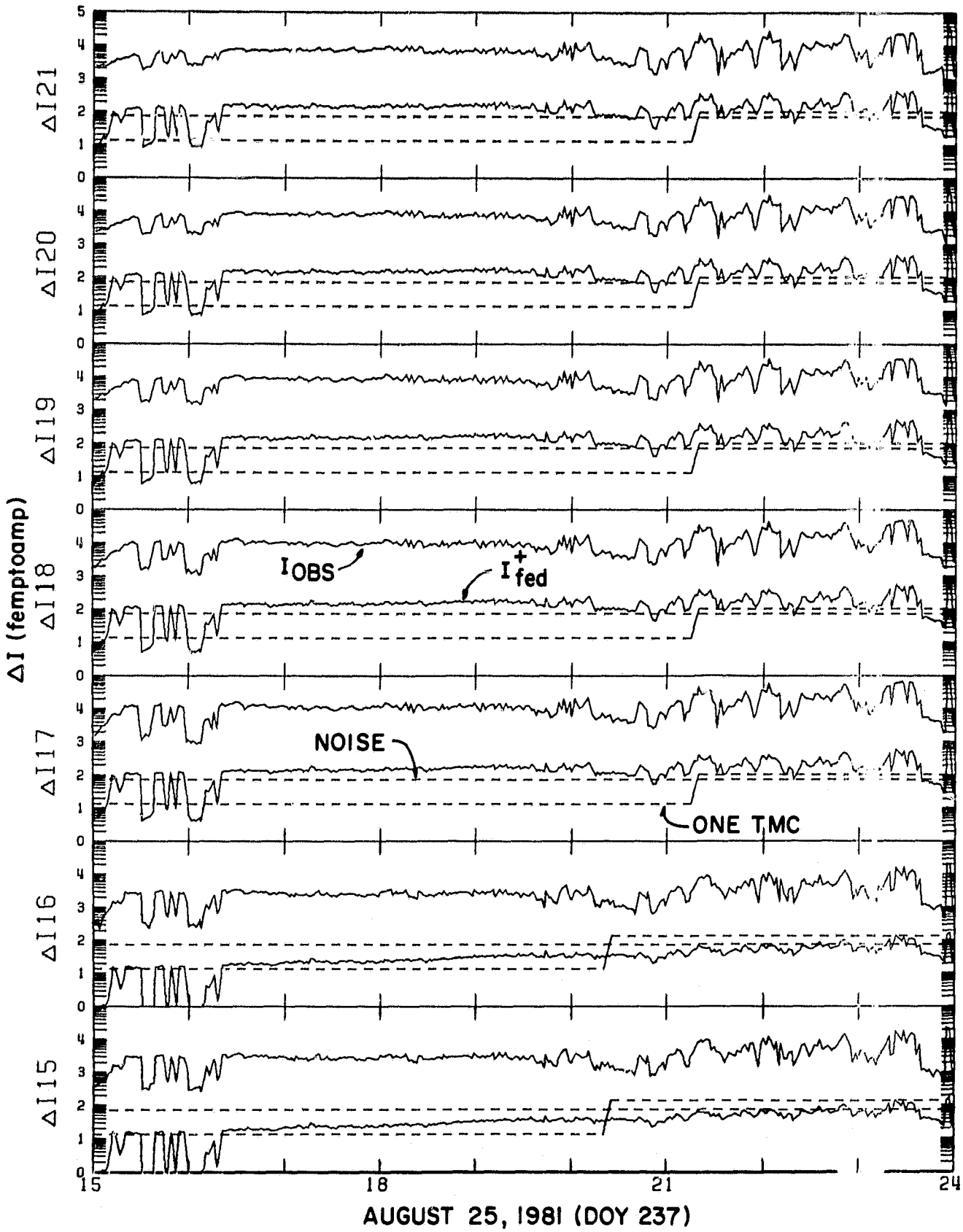

Figure 8c

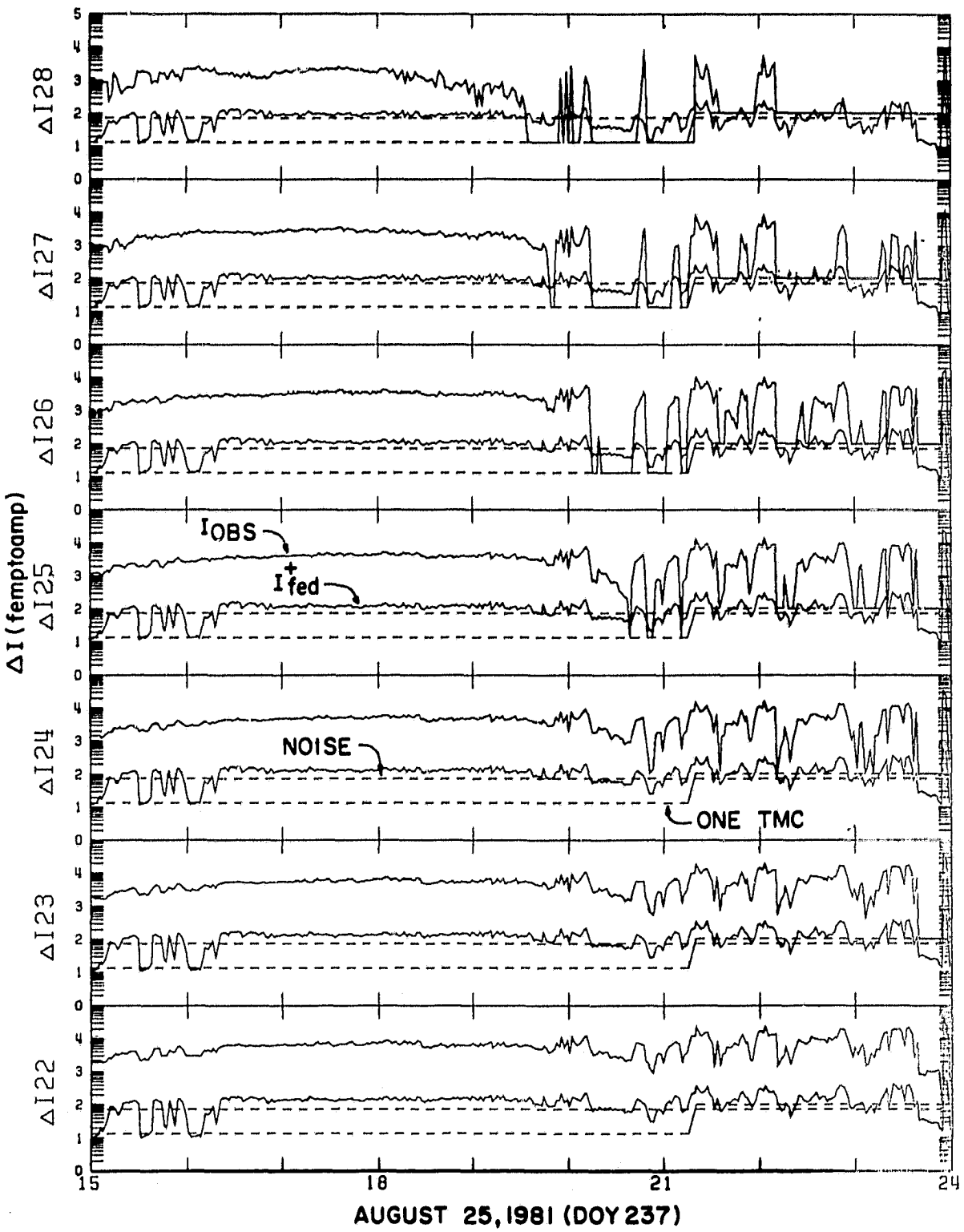

Figure 8d

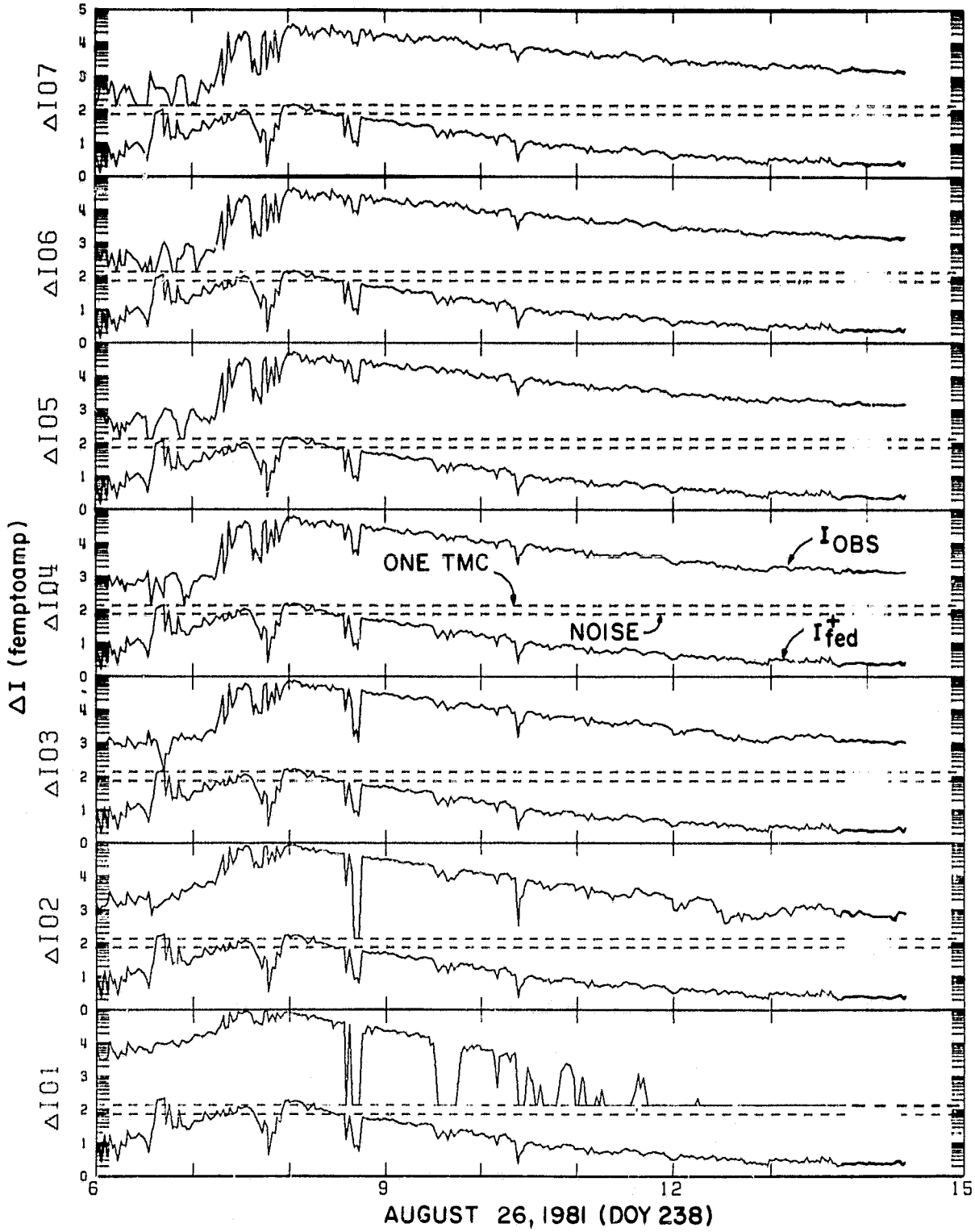

Figure 8e

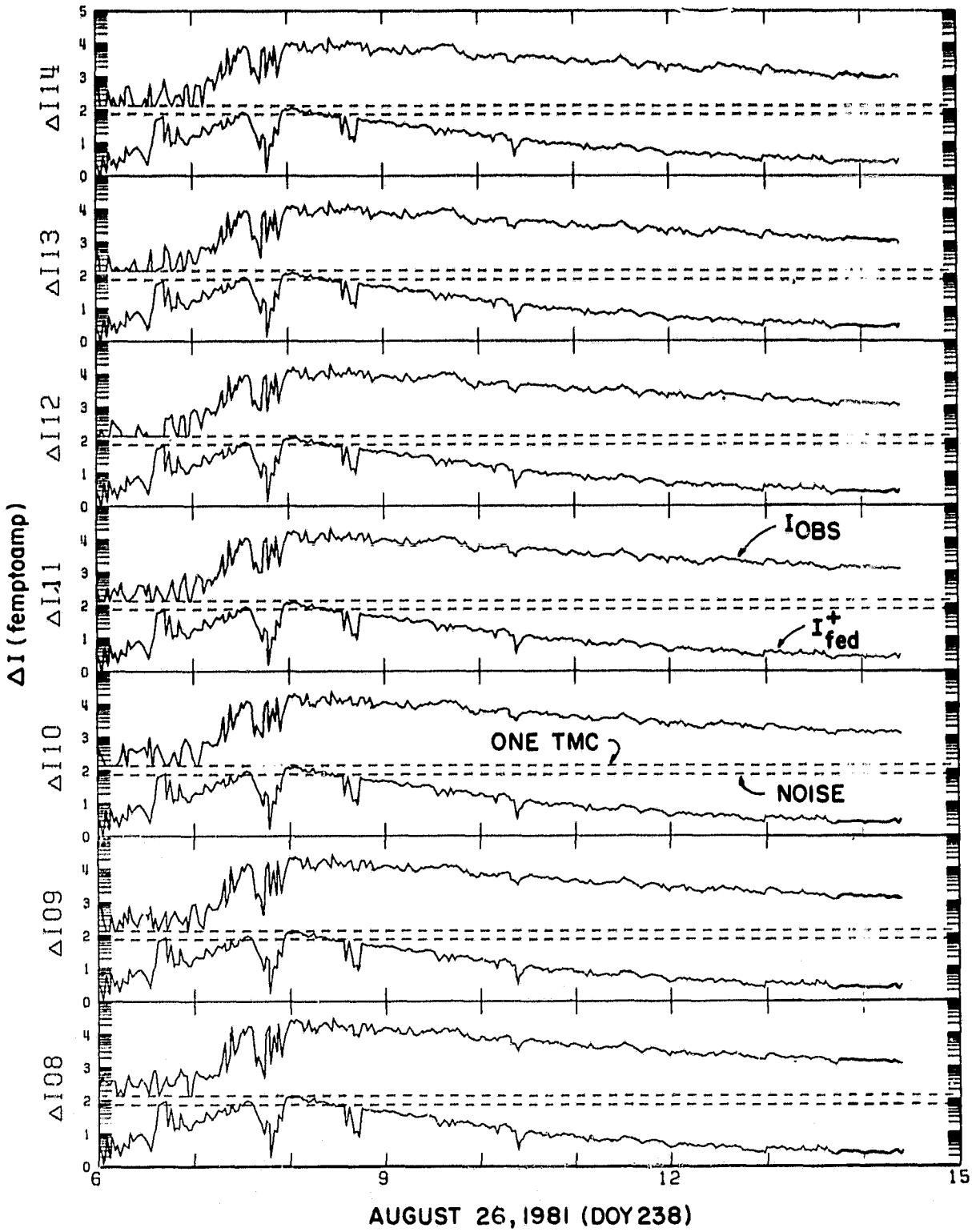

Figure 8f

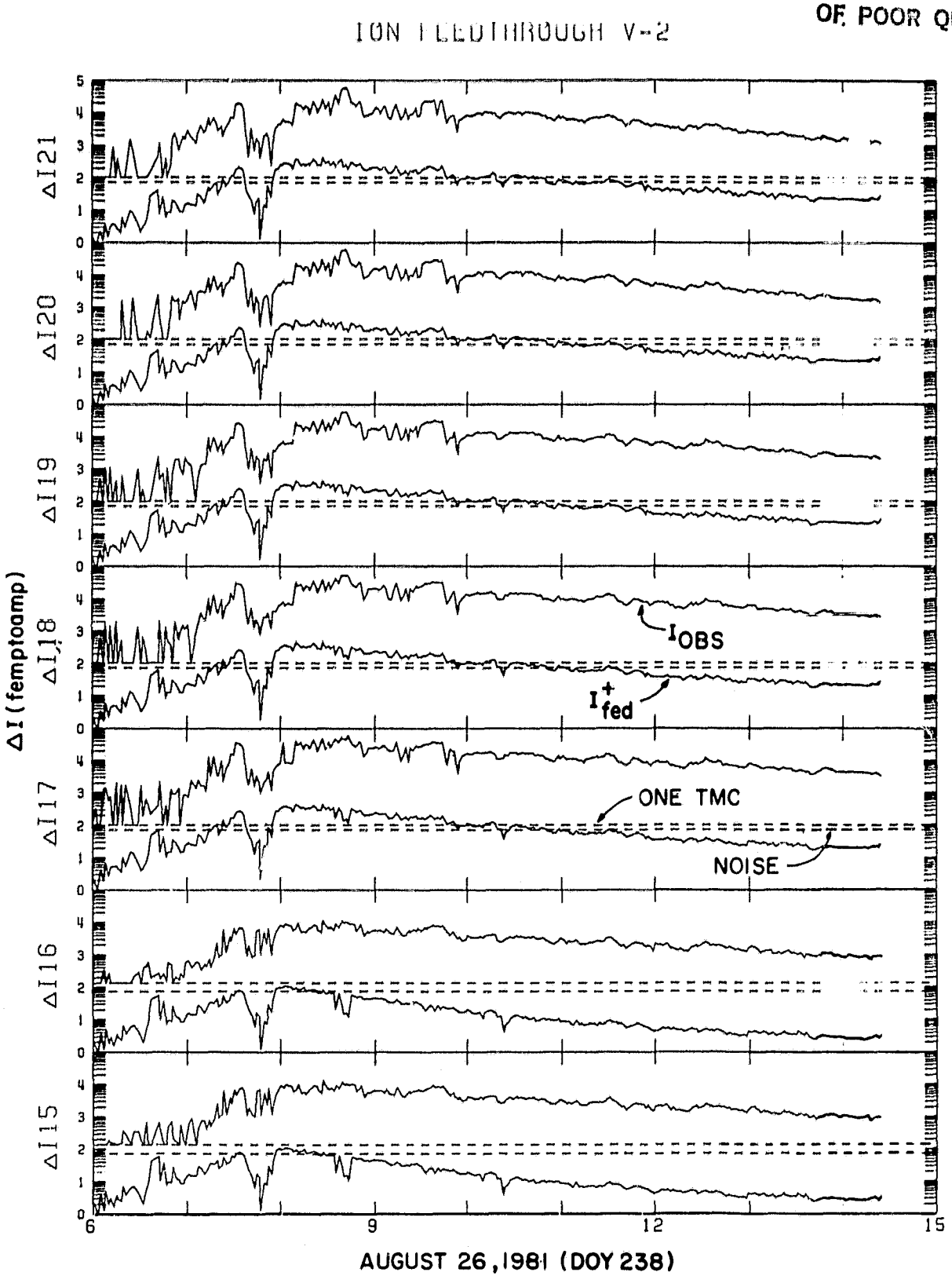

Figure 8g

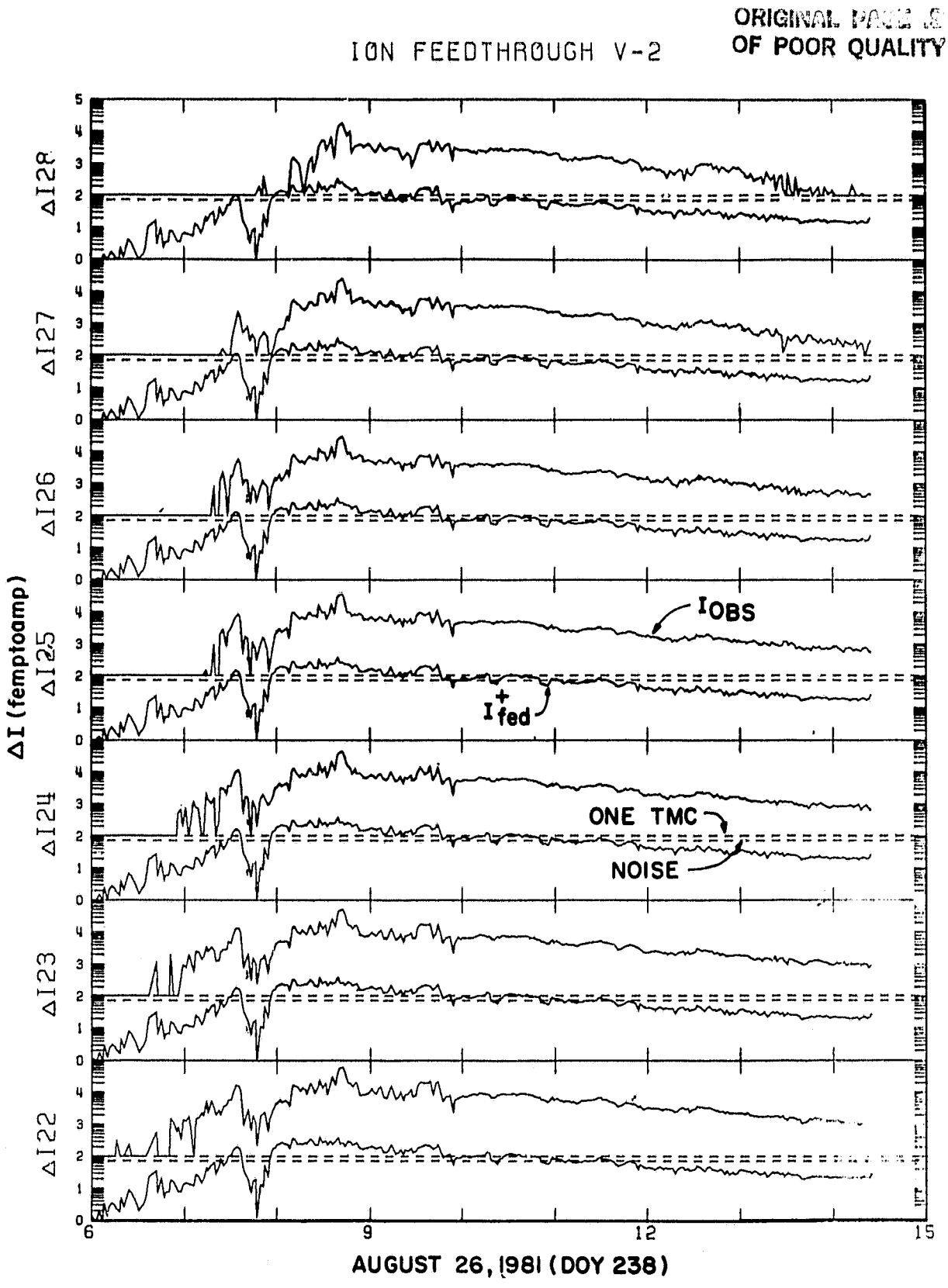

Figure 8h

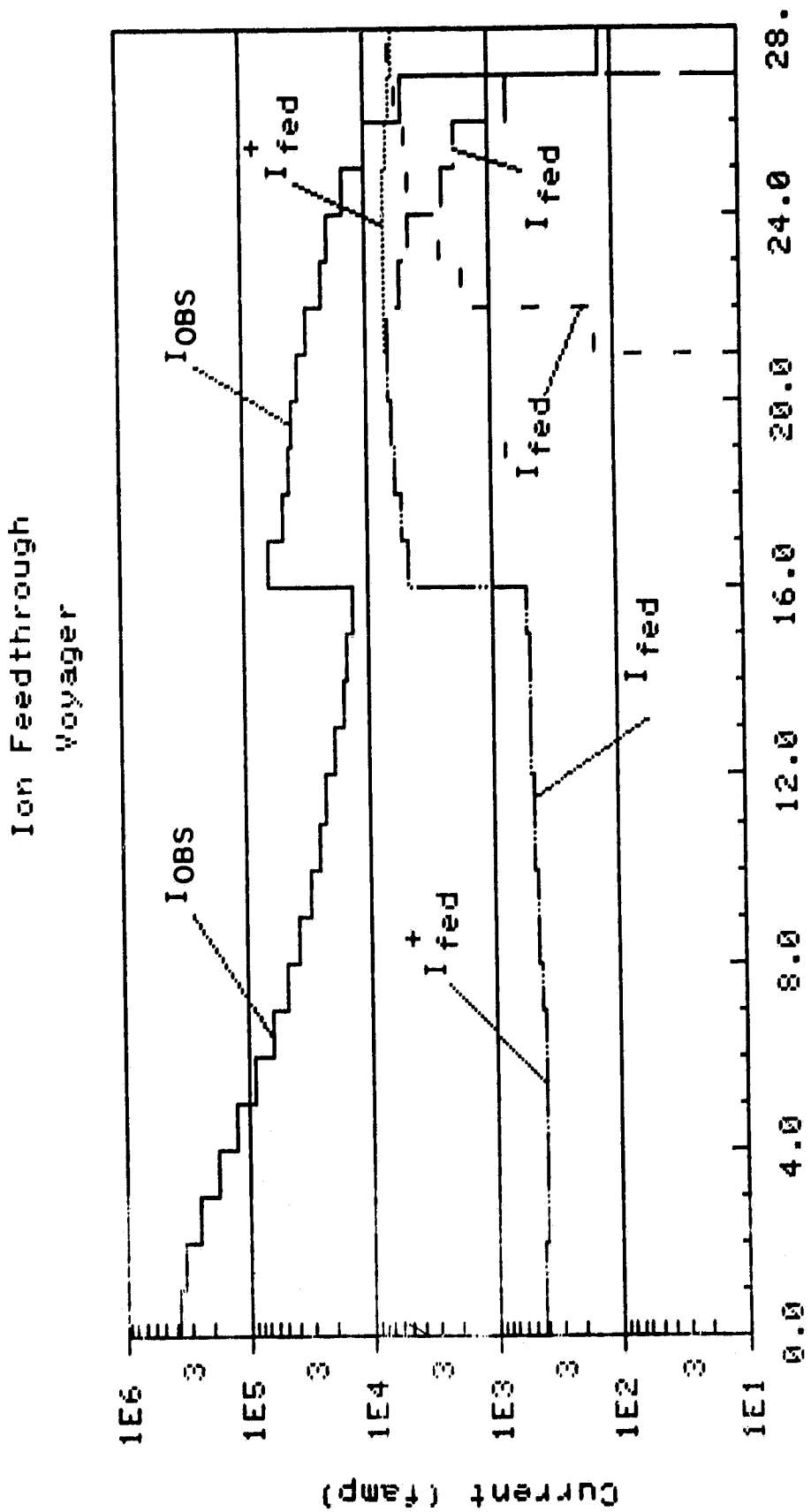

Figure 9